iScience

CellPress
OPEN ACCESS

Article

Nde1 is required for heterochromatin compaction and stability in neocortical neurons

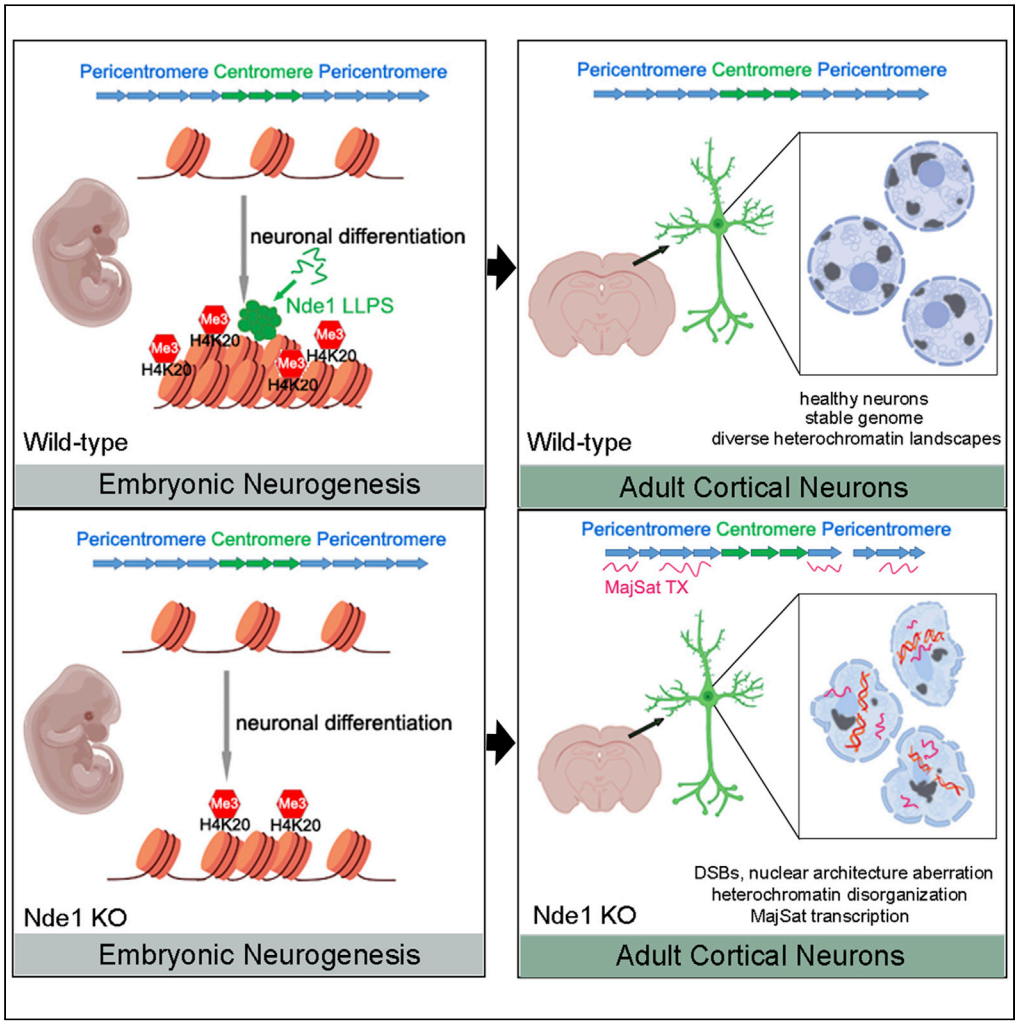

Alison A. Chomiak, Yan Guo, Caroline A. Kopsidas, ..., Qiong Zhou, Martin L. Doughty, Yuanyi Feng

yuanyi.feng@usuhs.edu

Highlights

Cortical neurogenesis is coupled with heterochromatin compaction marked by H4K20me3

Nde1 undergoes liquid-liquid phase separation and interacts with heterochromatin

Nde1 mutations impair H4K20me3 during neural progenitor differentiation

Neurons lacking Nde1 derepress heterochromatin and lose nuclear and genomic integrity

Chomiak et al., iScience *25*, 104354
June 17, 2022
https://doi.org/10.1016/j.isci.2022.104354

iScience

CellPress
OPEN ACCESS

Article

Nde1 is required for heterochromatin compaction and stability in neocortical neurons

Alison A. Chomiak,[1,6] Yan Guo,[1,7] Caroline A. Kopsidas,[2] Dennis P. McDaniel,[3] Clara C. Lowe,[2,8] Hongna Pan,[2,9] Xiaoming Zhou,[4] Qiong Zhou,[5] Martin L. Doughty,[5] and Yuanyi Feng[2,10,*]

SUMMARY

The *NDE1* gene encodes a scaffold protein essential for brain development. Although biallelic *NDE1* loss of function (LOF) causes microcephaly with profound mental retardation, *NDE1* missense mutations and copy number variations are associated with multiple neuropsychiatric disorders. However, the etiology of the diverse phenotypes resulting from *NDE1* aberrations remains elusive. Here we demonstrate Nde1 controls neurogenesis through facilitating H4K20 trimethylation-mediated heterochromatin compaction. This mechanism patterns diverse chromatin landscapes and stabilizes constitutive heterochromatin of neocortical neurons. We demonstrate that NDE1 can undergo dynamic liquid-liquid phase separation, partitioning to the nucleus and interacting with pericentromeric and centromeric satellite repeats. Nde1 LOF results in nuclear architecture aberrations and DNA double-strand breaks, as well as instability and derepression of pericentromeric satellite repeats in neocortical neurons. These findings uncover a pivotal role of NDE1/Nde1 in establishing and protecting neuronal heterochromatin. They suggest that heterochromatin instability predisposes a wide range of brain dysfunction.

INTRODUCTION

Although the expansion of cerebrum size is one of the most discernible characteristics of mammalian evolution, the increased number of cortical neurons is not sufficient to account for the increased intellectual capacities of the human brain. Along with this notion, genetic conditions that affect the generation of cortical neurons may lead to similar reductions in brain size but with distinctive cognitive outcomes. In contrast to some microcephaly (small brain) conditions with preserved cognition (Rauch et al., 2008; Rossi et al., 1987; Willems et al., 2010), biallelic loss of function (LOF) mutations of *NDE1* (NudE neurodevelopment protein 1) cause profound mental retardation (Alkuraya et al., 2011; Bakircioglu et al., 2011; Guven et al., 2012; Paciorkowski et al., 2013). Although the near-completely diminished brain function resulting from severe NDE1 deficiency is attributed to the substantial loss of neurons, individuals carrying missense mutations of *NDE1* or copy number variations (CNVs) of the *NDE1* gene locus 16p13.11 do not present changes in brain size, yet they show increased risk of multiple neuropsychiatric disorders, which include intellectual disability, epilepsy, autism, schizophrenia, and attention-deficit hyperactive disorder (Allach El Khattabi et al., 2020; Hannes et al., 2009; Ingason et al., 2011; Kimura et al., 2015; Nagamani et al., 2011; Ramalingam et al., 2011; Tropeano et al., 2013; Ullmann et al., 2007; Williams et al., 2010). The wide spectrum of brain morphological and functional impairments associated with altered *NDE1* gene dosage and function indicates that NDE1 acts beyond simply determining the quantity of neurons. However, the cellular and molecular mechanisms that underlie the diverse brain functional deficits resulting from *NDE1* LOF remain undefined.

The *NDE1* gene encodes a dynamic scaffold molecule that can be partitioned into various subcellular compartments in a context-dependent manner (Feng et al., 2000; Feng and Walsh, 2004; Lanctot et al., 2013; Pawlisz and Feng, 2011). Notably, the phenotype of NDE1/Nde1 LOF in both humans and mice preferentially affects the CNS, showing a prominent impact on neocortical neurogenesis (Alkuraya et al., 2011; Bakircioglu et al., 2011; Feng and Walsh, 2004; Guven et al., 2012). Despite the marked loss of layer II/III neurons of the neocortex, homozygous Nde1 knockout ($Nde1^{-/-}$) mice showed little anatomical changes in other brain structures such as the hippocampus, striatum, and cerebellum (Feng and Walsh, 2004). We

[1]Department of Neurology, Northwestern University Feinberg School of Medicine, 303 E. Superior Street, Chicago, IL 60611, USA

[2]Department of Biochemistry and Molecular Biology, Uniformed Services University, 4301 Jones Bridge Road, Bethesda, MD 20814, USA

[3]Biomedical Instrumentation Center, Uniformed Services University, 4301 Jones Bridge Road, Bethesda, MD 20814, USA

[4]Department of Medicine, Uniformed Services University, 4301 Jones Bridge Road, Bethesda, MD 20814, USA

[5]Department of Anatomy, Physiology, and Genetics, Uniformed Services University, 4301 Jones Bridge Road, Bethesda, MD 20814, USA

[6]Present address: Department of Epigenetics, Van Andel Institute, 333 Bostwick Ave. NE, Grand Rapids, MI 49503, USA

[7]Present address: Department of Oncology, Zhengzhou University People's Hospital, 8 Weiwu Road, Zhengzhou, P.R.C.

[8]Present address: Wake Forest University School of Medicine, 475 Vine St, Winston-Salem, NC 27101, USA

[9]Present address: National Institute on Alcohol Abuse and Alcoholism, 5625 Fishers Lane, Rockville MD 20852, USA

[10]Lead contact

*Correspondence: yuanyi.feng@usuhs.edu

https://doi.org/10.1016/j.isci.2022.104354

have shown previously that the neocortical-specific neuronal loss was a direct consequence of Trp53-dependent apoptosis, which was triggered by DNA double-strand breaks (DSBs) in those Nde1$^{-/-}$ neural progenitor cells (NPCs) that underwent the transition from multipotent to neuronal-fate-restrictive differentiations at the onset of cortical neurogenesis (Houlihan and Feng, 2014). More specifically, our cell cycle analysis showed that DSBs in Nde1$^{-/-}$ NPCs arose from stalled replication of heterochromatin DNA in mid to late S-phase (Houlihan and Feng, 2014). The establishment of heterochromatin regions is fundamental to stem cell differentiation, and it reshapes the nuclear landscape to allow the spatial segregation of chromatin domains with distinctive transcription activities (Craig, 2005; Noma et al., 2001; Sridharan et al., 2013; Talbert and Henikoff, 2006). Therefore, stalled heterochromatin DNA replication in neuronal fate-restrictive cell cycles of Nde1$^{-/-}$ NPCs suggested that NDE1/Nde1 plays a pivotal role during necessary heterochromatin remodeling for neuronal differentiation.

Heterochromatin constitutes a large portion of the mammalian genome (Lander et al., 2001; Linhoff et al., 2015; Solovei et al., 2016; Vicient and Casacuberta, 2017). It is distinguished from the transcriptionally active and loosely packed euchromatin by forming condensed structures that are predominantly distributed near the nuclear periphery and the nucleoli. Although the formation of heterochromatin can be facultative, driven by developmental- and/or cell type-specific epigenetic transcriptional repression programs, the chromatin segments composed of tandem repeats of the centromere, pericentromere, subtelomere, and transposons must be silenced constitutively to maintain chromosome integrity and to prevent the genetic instability of these repetitive DNA elements (Allshire and Madhani, 2018; Saksouk et al., 2015; Vicient and Casacuberta, 2017). Despite a crucial role in genome maintenance and function, constitutive heterochromatin is the most poorly understood component of the eukaryotic genome, owing to difficulties in assessing its underlying repetitive DNA structures and the lack of genetic experimental models to study its formation *in vivo*, and its regulation and function.

Given the specific requirement of Nde1 in linking heterochromatin replication and genome protection to neuronal differentiation, we asked whether the multitude of phenotypes associated with *NDE1* aberrations originates from aberrant heterochromatin establishment, maintenance, stability, and/or function. In this study, we present evidence that neocortical neurogenesis is associated with trimethylation of histone H4 lysine 20 (H4K20me3), a histone posttranslational modification (PTM) that distinctively marks the constitutive heterochromatin, stabilizes the repetitive genomic sequences, and shapes diverse chromatin landscapes of cortical neurons. We demonstrate that stalled heterochromatic DNA replication in Nde1$^{-/-}$ NPCs was linked to compromised H4K20me3 and that Nde1 is an intrinsically disordered protein (IDP) that can undergo liquid-liquid phase separation, translocate to the nucleus, co-localize with H4K20me3 modified domains, and interact with centromeric and pericenteromeric heterochromatin. Furthermore, the nuclear entrance of NDE1 is directed by its partner BRAP, and mice with LOF of Nde1 and Brap phenocopy, both showing not only compromised H4K20me3 during cortical neurogenesis, but also DSBs and nuclear architecture and heterochromatin aberrations in adult neocortical neurons. The profound heterochromatin defects and derepression of pericentromeric satellite repeats resulting from Nde1 and Brap LOF coincided with progeria-like changes as well as neuroinflammation and neurodegenerative phenotypes in the cerebral cortical tissue. These data suggest that failures in heterochromatin remodeling during neurogenesis impairs the genome stability and vitality of neocortical neurons; and heterochromatin aberrations may underlie the cognitive dysfunction and multitude of neuropsychiatric phenotypes associated with *NDE1* aberrations.

RESULTS

Cerebral cortical neurogenesis requires heterochromatin compaction via H4K20me3

To test whether the role of NDE1 in cerebral cortex neurogenesis is associated with re-patterning heterochromatin in NPC differentiation, we first determined how heterochromatin is modified in neurogenesis. We analyzed PTMs on histones extracted from mouse embryonic cortical tissues over the course of cerebral cortex development by immunoblotting (IB). From the onset of cortical neurogenesis at embryonic day 12.5 (E12.5) to its completion at birth (P0), we found that the levels of histone H4 lysine 20 trimethylation (H4K20me3), histone H3 lysine 27 trimethylation (H3K27me3), and histone H2A ubiquitination (H2Aub) increased progressively in the cortical tissue (Figure 1A). The increases in H3K27me3 and H2Aub were expected for their roles in the suppression of polycomb-group genes and the establishment of facultative heterochromatin in neurodevelopment. However, the remarkable upregulation of H4K20me3 and corresponding down regulation of H4K20me1 was surprising. H4K20me3 is a repressive histone

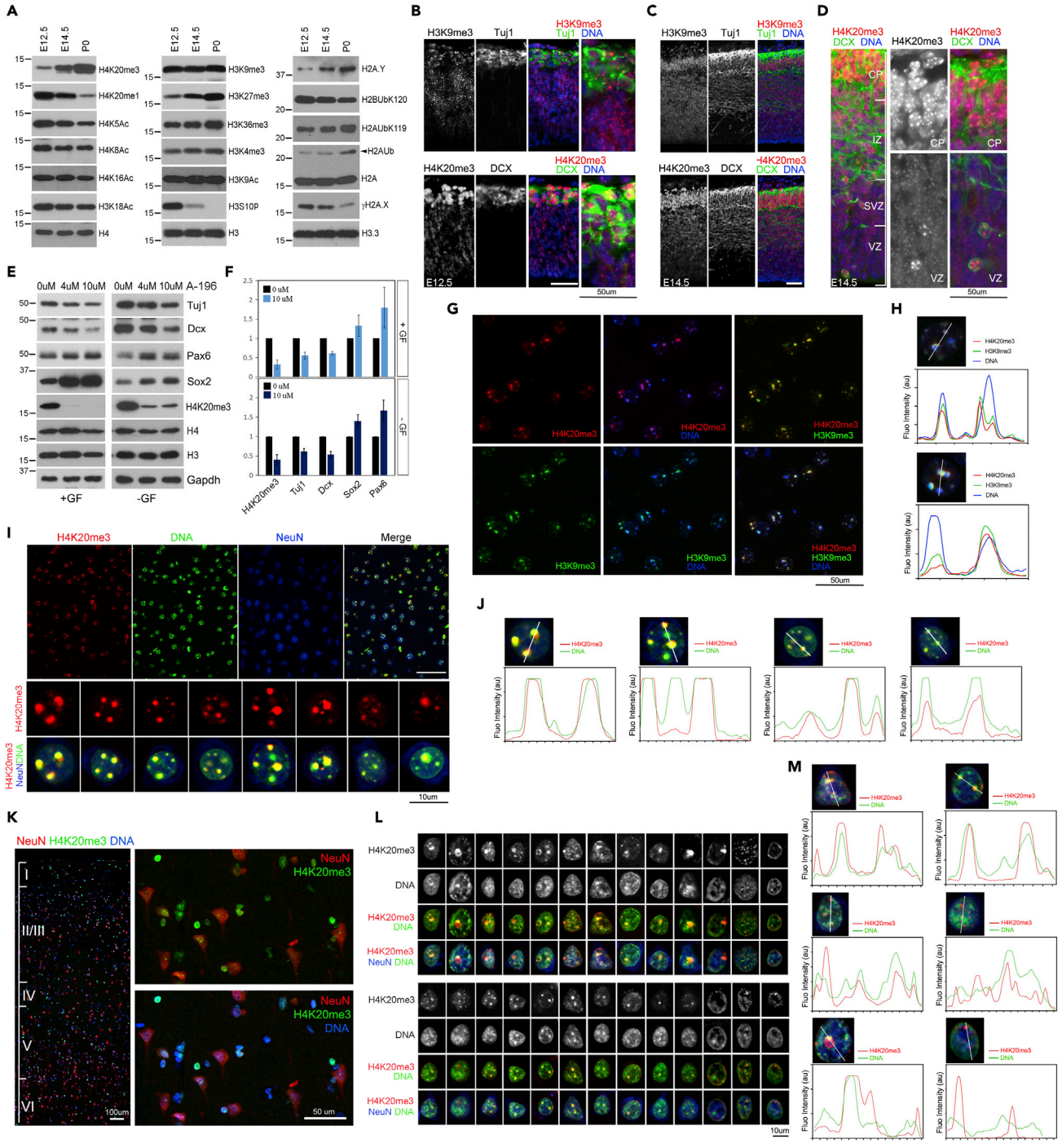

Figure 1. H4K20me3 modification of heterochromatin in neurogenesis yields diverse chromatin landscapes in neocortical neurons

(A) IB of histone extracts from developing murine cerebral cortical tissues at E12.5, E14.5, and P0. Note the progressive increase of H4K20me3, H3K27me3, and H2Aub during the course of cortical neurogenesis.

(B–D) IH analysis of embryonic cerebral cortical sections with antibodies against H3K9me3 and H4K20me3. Sections are co-stained with new neuron markers Tuj1 or DCX to reveal the intense H4K20me3 foci in neurons of the nascent cortical plate at E12.5 (B), as well as in DCX+ newborn neurons in the VZ/SVZ, IZ and CP at E14.5 (C, D). Bars: 100um or 50 um as indicated. VZ: ventricular zone; SVZ: subventricular zone; IZ: intermediate zone; CP: cortical plate.

(E and F) Representative IB images and quantifications (mean ± SD) of whole cell extracts from NPCs cultured in the presence or absence of growth factors (GFs). The cultures were treated with A-196 for 72 h at the indicated concentrations.

Figure 1. *Continued*

(G) Representative IH images of H4K20me3 (red)-H3K9me3 (green) double labeled neocortical sections of young adult mice. Nuclear DNA is stained by Hoechst 33,342 (blue). Bar: 50um.

(H) Line scan of H4K20me3, H3K9me3, and Hoechst 33,342 fluorescence intensities in selected nuclei of mouse neocortical tissue, showing the co-localization of H4K20me3 with chromocenter and heterochromatin domains marked by H3K9me3.

(I) Representative IH images of H4K20me3 (red)-NeuN (blue) double labeled neocortical sections of young adult mice. Nuclear DNA is stained by Hoechst 33,342 (green). Bar:50um.

(J) Line scan of H4K20me3 and Hoechst 33,342 fluorescence intensities in selected nuclear images of individual neocortical neurons. Note the diverse pattern of H4K20me3 distribution and occupancy with respect to chromocenters.

(K) Representative IH images of NeuN (red)-H4K20me3 (green) double stained postmortem human cortical sections. Bars: 100um or 50um as indicated.

(L) Selected nuclear images of individual neurons of postmortem human neocortical sections double stained by antibodies against H4K20me3 (red) and NeuN (blue). Nuclear DNA is stained by Hoechst 33,342 (green). Note the greater heterogeneity of H4K20me3 landscapes and differential coverage of nuclear DNA by H4K20me3 in human than in murine brains. Bars: 10um.

(M) Line scan of H4K20me3 and Hoechst 33,342 fluorescence intensities in selected nuclear images of human postmortem neocortical neurons, showing hyper-heterogeneity of differential H4K20me3 occupancy with respect to chromocenters. See also Figure S1.

modification enriched at the repetitive DNA elements of constitutive heterochromatin that are condensed in early stem cell differentiation and are expected to be stable throughout the cells' lifespan (Benetti et al., 2007; Jorgensen et al., 2013; Kidder et al., 2017; Saksouk et al., 2015; Schotta et al., 2004, 2008). The *de novo* establishment of constitutive heterochromatin requires epigenetic silencing by histone H3 lysine 9 trimethylation (H3K9me3), which is followed by H4K20me3 to further condense repetitive DNA elements and transposons to ensure their stability (Bierhoff et al., 2014; Jorgensen et al., 2013; Marion et al., 2009; Richards and Elgin, 2002; Schotta et al., 2008; Wongtawan et al., 2011). Consistent with this, we observed that the intensity of H3K9me3 foci was uniform in all cortical cells, but the intensity of H4K20me3 foci drastically increased in new neurons (Dcx+ or Tuj1+) compared to NPCs, even in those newborn neurons migrating from the ventricular zone to the cortical plate (Figures 1B–1D and S1A).

The remarkable increase in the intensity of H4K20me3 foci in newborn neurons prompted us to further ask whether H4K20me3 is required for neurogenesis. Tri- and di-methylation of lysine 20 in histone H4 is catalyzed by the histone methyltransferases Suv420h1 (KMT5B) and Suv420h2 (KMT5C) (Hahn et al., 2013; Schotta et al., 2008). We thus applied A-196, a potent and selective inhibitor of Suv420h1 and Suv420h2 (Bromberg et al., 2017), to NPC cultures and tested its effect on neuronal differentiation. We found that A-196 decreased the levels of new neuron makers Dcx and Tuj1 while increasing the levels of pro-NPC makers Pax6 and Sox2. This effect of A-196 on impeding neurogenesis was observed in both basal NPC cultures with low degrees of spontaneous neuronal differentiation and upon the induction of neuronal differentiation by growth factor withdrawal (Figures 1E and 1F). Given that chromatin compaction by H4K20me3 is essential for heterochromatin stabilization, the concomitant increase of H4K20me3 in neurogenesis is likely necessary for post-mitotic neurons to gain life-long protection of repetitive sequences of the genome.

H4K20me3 marks diverse chromatin landscapes in neocortical neurons

We further found that H4K20me3 not only compacts heterochromatin but also marks a wide array of chromatin landscapes of neocortical neurons. In these neurons, we observed that H4K20me3 foci largely overlapped with both the H3K9me3 condensates and the chromocenters containing AT-rich satellite repeats that are stained intensively by the DNA dye Hoechst (Guenatri et al., 2004) (Figures 1G, 1H, and S1B). Furthermore, we found that, among neocortical neurons, H4K20me3-modified chromatin exhibited variable patterns and occupied deferent domains of the nucleus (Figures 1I and 1J). This suggests that H4K20me3 shapes diverse chromatin landscapes in various neurons besides reinforcing the compaction of the highly repetitive DNA elements to strengthen chromosome stability.

To further assess the association of H4K20me3 with the diversification of heterochromatin landscapes in neocortical neurons, we examined the distribution of H4K20me3 marked nuclear domains in human cerebral cortical tissue with the perception that there is a substantial increase in the diversity of neocortical neurons from mice to humans. Similar to what was observed in mice, H4K20me3-modified heterochromatin exhibited condensates of variable size throughout the nucleus of human cortical neurons (Figures 1K, 1L, and S1C). These condensates were enriched in the characteristic heterochromatin domains, showing preferential association with nuclear lamina and nucleoli (Figure 1L). However, the H4K20me3 landscape in human neurons is much more heterogeneous than in murine neurons. In human neurons, H4K20me3 condensates showed a wider size range, occupied various nuclear territories, and displayed differential

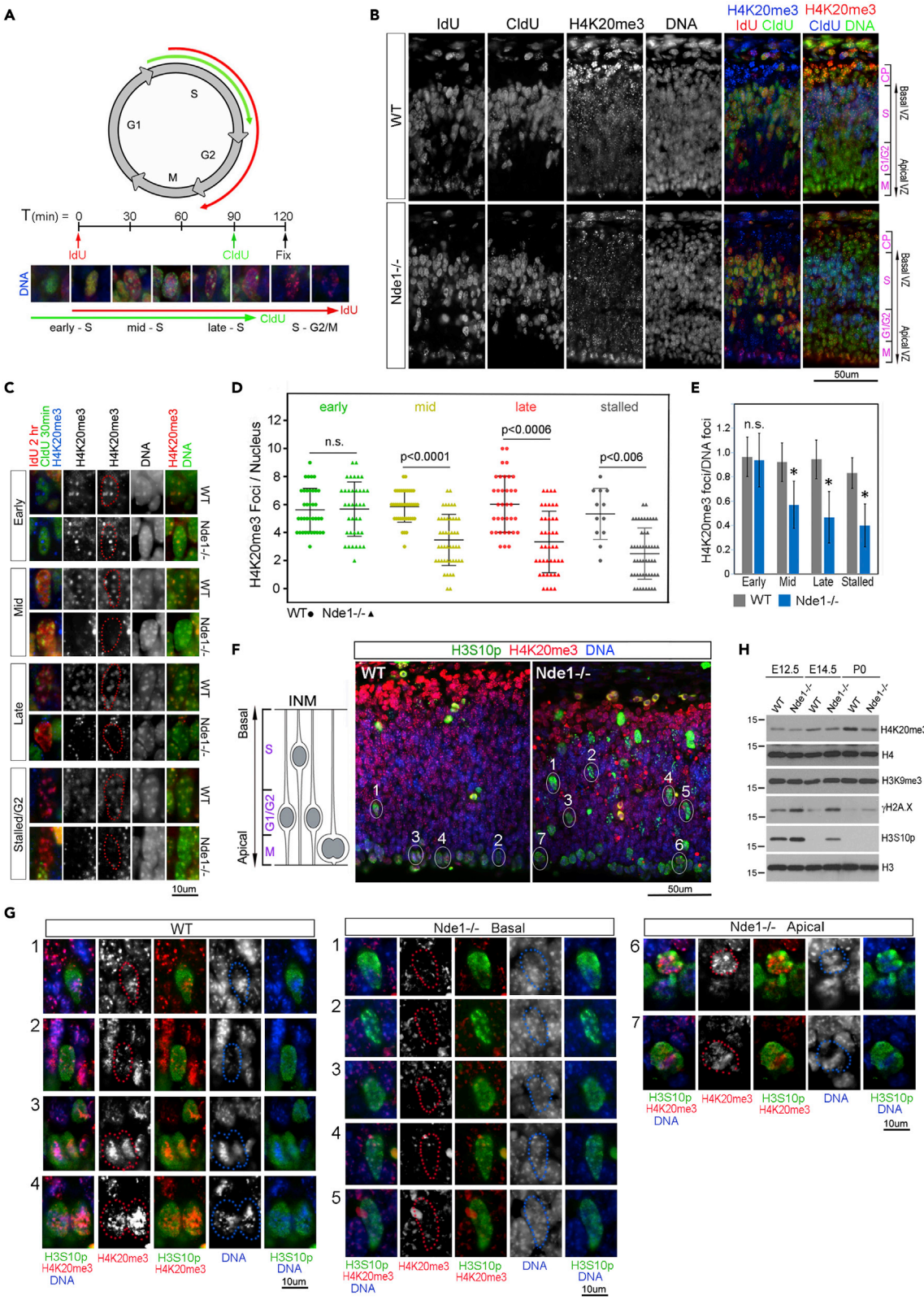
A
S
G1
G2
M
T (min) = 0 30 60 90 120
IdU
CldU
Fix
DNA
early - S
mid - S
late - S
S - G2/M
B
IdU
CldU
H4K20me3
DNA
H4K20me3 IdU CldU
H4K20me3 CldU DNA
WT
Nde1-/-
CP
S
G1/G2
M
Basal VZ
Apical VZ
50um
C
IdU 2 hr
CldU 30min
H4K20me3
H4K20me3
H4K20me3
DNA
H4K20me3
DNA
Early
Mid
Late
Stalled/G2
WT
Nde1-/-
10um
D
early
mid
late
stalled
H4K20me3 Foci / Nucleus
n.s.
p<0.0001
p<0.0006
p<0.006
WT● Nde1-/-▲
E
H4K20me3 foci/DNA foci
n.s.
Early
Mid
Late
Stalled
WT
Nde1-/-
F
H3S10p H4K20me3 DNA
INM
Basal
Apical
S
G1/G2
M
WT
Nde1-/-
50um
H
E12.5 E14.5 P0
WT
Nde1-/-
H4K20me3
H4
H3K9me3
γH2A.X
H3S10p
H3
G
WT
Nde1-/- Basal
Nde1-/- Apical
H3S10p
H4K20me3
DNA
10um

Figure 2. Stalled DNA replication, DSBs and G2/M arrests of Nde1$^{-/-}$ NPCs are associated with compromised H4K20me3

(A) Diagram of IdU-CldU sequential labeling scheme for analyzing S-phase progression in embryonic cortical tissue. Pregnant dams were given IdU followed by CldU before embryos were fixed at E12.5. Embryonic NPCs were analyzed by IdU-CldU double IH staining. DNA were stained by Hoechst 33,342.

(B) Representative IH images of H4K20me3 in S-phase cortical NPCs of WT and Nde1$^{-/-}$embryos sequentially labeled by IdU and CldU as described in (A). DNA were stained by Hoechst 33,342. VZ: ventricular zone; CP: cortical plate; S: S-phase zone; G2/M: G2 and M-phase zone. Bar: 50um.

(C) Representative IH images of H4K20me3 in NPCs at early S-phase (IdU-;CldU+), mid S-phase (IdU+;CldU+), late S-phase (IdU+; sparse CldU+ foci), or stalled S-phase (IdU+; CldU- and in the S-phase zone of basal VZ as opposed to where G2/M nuclei localize at the apical VZ) at E12.5. DNA were stained by Hoechst 33,342. H4K20me3 and Hoechst 33,342 double stained images are included to reveal the H4K20me3 occupancy at chromocenters. Nuclear territory is marked by red dots on H4K20me3 images according to DNA stains by Hoechst 33,342 (middle column). Note the weak and diffuse H4K20me3 immunosignals in late S-phase and DNA replication-stalled Nde1$^{-/-}$ NPCs. Bar: 10um.

(D) Numbers of H4K20me3+ foci per nucleus in NPCs of E12.5 embryos at early, mid, late, and stalled S-phase (mean ± SD). p values by two-sample Kolmogorov-Smirnov tests are indicated.

(E) Ratios of H4K20me3 to Hoechst 33,342+ foci in nuclei of early, mid, and late S-phase or DNA replication stalled cortical NPCs at E12.5. Mean ± SD *p< 0.0001, by student's t tests.

(F) Representative IH images of E12.5 cortical sections that were doubled labeled by antibodies against phospho-Histone H3 Ser10 (H3S10p, in green) and H4K20me3 (in red). DNA was stained by Hoechst 33,342 (in blue). Diagram to the left illustrates cell cycle-dependent interkinetic nuclear migration (INM) of cortical NPCs. Bar: 50um.

(G) High-magnification IH images of H4K20me3 in selected H3S10p+ nuclei shown in (F) (indicated by circles and numbers). Note the reduced number and intensity of H4K20me3 foci in Nde1−/− nuclei retained in basal ventricular zone. Bar:10um.

(H) IB of histone extracts from cortical tissue at E12.5, E14.5 and P0, showing that Nde1 LOF results in decreased H4K20me3 with increased DSBs (γH2A.X) and G2/M arrest (H3S10p). See also Figure S2.

coverage of the Hoechst-stained chromocenter DNA (Figures 1L and 1M). These variations in the abundance and distribution of H4K20me3 modified chromatin domains increase the epigenetic diversity, which may add a new dimension to the multidimensional characteristics of neocortical neurons and allow for an extraordinarily wide spectrum of chromatin landscapes to be established in neurons of the human cerebrum.

Stalled DNA replication in Nde1$^{-/-}$ NPCs is coupled with H4K20me3 deficiency

Given the critical association of H4K20me3 with heterochromatin compaction in neocortical neurogenesis, we next determined whether defects in H4K20me3 underlie stalled heterochromatin replication that we previously observed in Nde1$^{-/-}$ NPCs (Houlihan and Feng, 2014). DNA replication in S-phase starts with euchromatin and ends with heterochromatin. To determine where in S or G2 phase NPCs were, we labeled the NPCs progressing through S-phase by IdU-CldU sequential administrations to pregnant dams at E12.5 (Figure 2A). We then compared the number of H4K20me3-dense foci relative to the number of Hoechst-intense chromocenters in IdU and CldU labeled NPCs at early (IdU-;CldU+), mid (IdU+;CldU+), and late S-phase (IdU+; sparse CldU+ foci), respectively. Compared to WT NPCs, Nde1$^{-/-}$ NPCs' nuclei in S-phase exhibited an overall reduction in the intensity and number of H4K20me3 foci relative to the number of chromocenters (Figure 2B). By quantifying the numbers of H4K20me3 foci per chromocenter or per cell with respect to S-phase progression, we found that the numbers were comparable between WT and Nde1$^{-/-}$ NPCs in early S-phase but were significantly reduced in Nde1$^{-/-}$ NPCs in the mid and late S-phase or in those that showed stalled DNA replication (IdU+;CldU-, and localized in the S-phase zone)(Figures 2C–2E). This result indicates that stalled heterochromatin DNA replication in Nde1$^{-/-}$ NPCs was tightly coupled to compromised heterochromatin remodeling though H4K20me3, a necessary PTM for neuronal differentiation and genome protection.

A characteristic phenotype shown by Nde1$^{-/-}$ NPCs was the mis-localization of mitotic nuclei and skewed mitotic spindles (Feng and Walsh, 2004). Given that constitutive heterochromatin encompasses primarily the centromere and pericentromere regions, we next sought to determine whether such mitotic defects of Nde1$^{-/-}$ NPCs could arise from aberrant H4K20me3 modification in heterochromatin replication before G2/M phase. NPCs in WT embryos are known to undergo interkinetic nuclear migration (INM) and localize their nuclei at the apical end adjacent to the brain ventricles during mitosis (Takahashi et al., 1993), but mitotic nuclei of Nde1$^{-/-}$ NPC frequently failed to localize at the apical end (Feng and Walsh, 2004). We, therefore, immuno-labeled mitotic NPCs by phospho-histone H3 Ser10 (H3S10p) and examined H4K20me3 in these cells. We found that H4K20me3 was largely condensed in H3S10p-labeled WT and those Nde1$^{-/-}$ nuclei that were appropriately localized to the apical end. However, the H4K20me3 foci were substantially weakened, reduced in numbers, or absent in those H3S10p-labeled Nde1$^{-/-}$ NPCs with basally mis-localized nuclei (Figures 2F and 2G). This strongly suggested that the mitotic defects in Nde1$^{-/-}$ NPCs were coupled to compromised H4K20me3 in late S-phase.

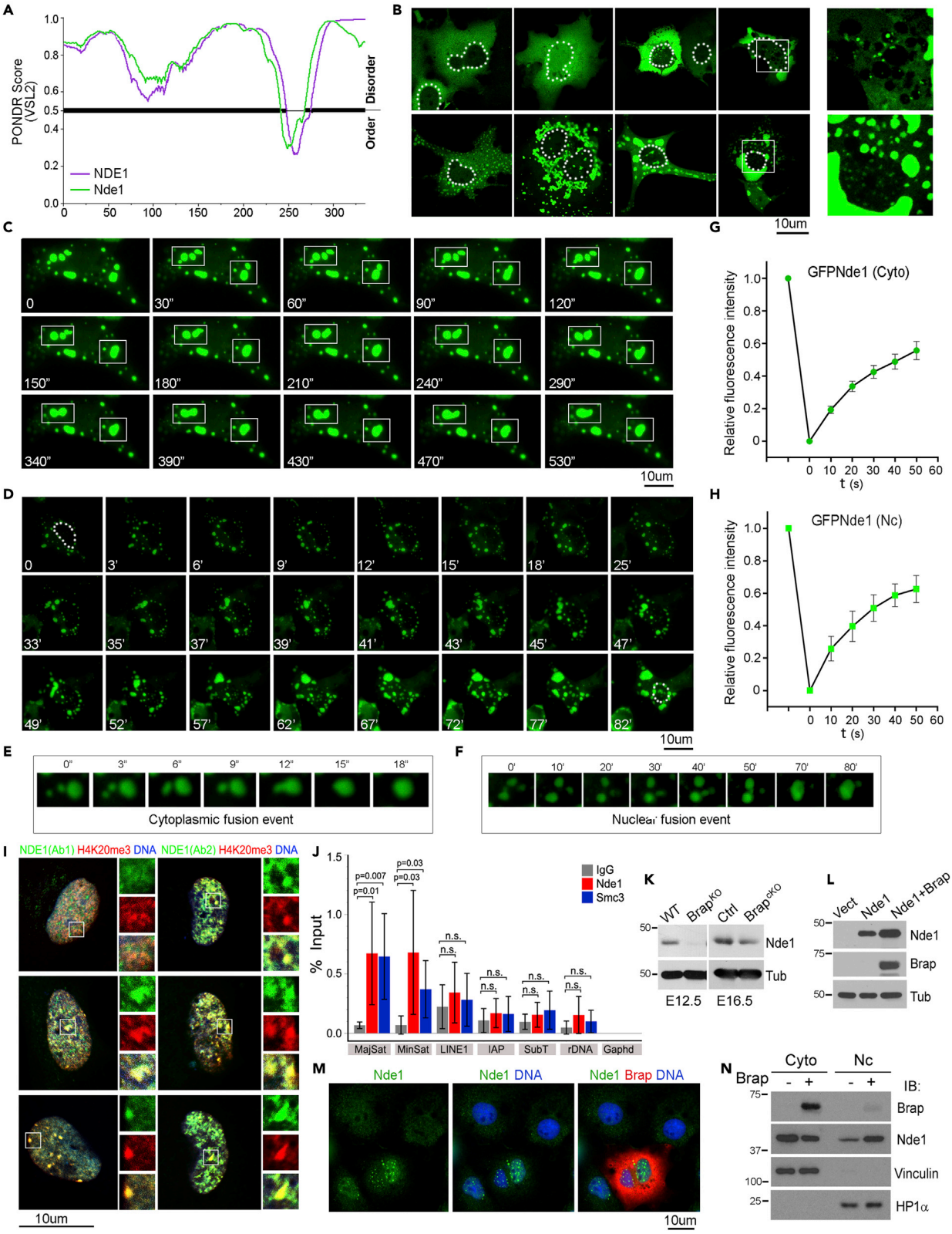
A
PONDR Score (VSL2)
Disorder
Order
NDE1
Nde1
B
10um
C
0
30"
60"
90"
120"
150"
180"
210"
240"
290"
340"
390"
430"
470"
530"
10um
G
GFPNde1 (Cyto)
Relative fluorescence intensity
t (s)
D
0
3'
6'
9'
12'
15'
18'
25'
33'
35'
37'
39'
41'
43'
45'
47'
49'
52'
57'
62'
67'
72'
77'
82'
10um
H
GFPNde1 (Nc)
Relative fluorescence intensity
t (s)
E
Cytoplasmic fusion event
F
Nuclear fusion event
I
NDE1(Ab1) H4K20me3 DNA
NDE1(Ab2) H4K20me3 DNA
10um
J
% Input
IgG
Nde1
Smc3
p=0.007
p=0.01
p=0.03
p=0.03
n.s.
MajSat
MinSat
LINE1
IAP
SubT
rDNA
Gaphd
K
WT
Brap^KO
Ctrl
Brap^cKO
Nde1
Tub
E12.5
E16.5
L
Vect
Nde1
Nde1+Brap
Nde1
Brap
Tub
M
Nde1
Nde1 DNA
Nde1 Brap DNA
10um
N
Cyto
Nc
Brap
IB:
Brap
Nde1
Vinculin
HP1α

Figure 3. Nde1 is an IDP that can form spherical condensates through LLPS and directed to the nucleus by Brap

(A) Intrinsic disordered regions of human NDE1 and murine Nde1 proteins (by Predictor of Natural Disordered Regions). VSL2 scores are shown on the y axis, and amino acid positions are shown on the x axis.

(B) Fluorescence confocal microscopy images of EGFP-Nde1 expressed in Cos7 cells, revealing the variety of distribution patterns. The position of the nucleus is marked by dotted lines, high-magnification images of the boxed areas are included. Bar:10um.

(C) Time-lapse images of Cos7 cells expressing EGFP-Nde1 (laser excitation every 10 s for the time indicated), showing dynamic fusion and redistribution. The position of the nucleus is marked on the panel of t = 0. Bar: 10um.

(D) Time-lapse images of Cos7 cells expressing EGFP-Nde1 (laser excitation every 10 min for the time indicated), showing the nuclear import and the formation of nuclear condensates. The position of the nucleus is marked on panels of t = 0 and t = 82′, respectively.Bar:10um.

(E) An example of droplet fusion event of cytoplasmic EGFP-Nde1.

(F) An example of droplet fusion event of nuclear EGFP-Nde1.

(G) FRAP of cytoplasmic GFP-Nde1 condensates. Shown is the signal intensity (mean ± SD, n = 7) relative to the pre-bleaching signal (y axis) versus time relative to photo-bleaching (x axis).

(H) FRAP of nuclear GFP-Nde1 condensates. Shown is - signal intensity (mean ± SD, n = 7) relative to the pre-bleaching signal (y axis) versus time relative to photo-bleaching (x axis).

(I) Super-resolution immunofluorescence confocal microscopic images of human neural stem/progenitor cells co-stained with antibodies against H4K20me3 (red) and NDE1. Shown were representative images of two polyclonal anti-NDE1 antibodies. Ab1 is against the N-terminus and Ab2 is against full-length NDE1 protein. Note the strong co-localization of NDE1 with condensed H4K20me3 chromatin shown by both antibodies. Bar:10um.

(J) Results of Nde1 and Smc3 ChIP qPCR analyses from mouse embryonic E12.5 cortical tissue. A non-specific rabbit IgG antibody was used as the negative control. Shown are data from a minimum of three independent preparations of chromatin as percent of the input (Mean ± SD) with p values of student's t tests.

(K) IB analysis of embryonic cerebral cortical tissue of $Brap^{KO}$ ($Brap^{-/-}$) and $Brap^{cKO}$ mice and their WT or control littermates, showing that the level of Nde1 protein is decreased by Brap abrogation. This indicates the requirement of Brap for the stability of Nde1.

(L) IB analysis of whole protein extracts from HEK293 cells transfected by recombinant Nde1 and Brap, revealing that the level of Nde1 is enhanced by Brap expression.

(M) A representative IF image of Cos 7 cells transfected by recombinant Brap and double stained with antibodies against Nde1 (green) and Brap (red). Nuclear DNA is stained by Hoechst 33,342 (blue). It demonstrates that the nuclear localization of endogenous Nde1 is enhanced in cells with Brap over-expression. Bar:10um.

(N) Cell fractionation and IB analyses of Cos7 cells transfected with recombinant Nde1 and Brap, showing increased Nde1 in the nuclear fraction of cells with Brap expression. See also Figure S3 and Video S1, Fluorescence images related to Figure 3C, Video S2, Phase contrast images related to Figure 3C, Video S3, Fluorescence images related to Figure 3E, and Video S4, Phase contrast images related to Figure 3E.

We confirmed that the overall level of H4K20me3 was reduced in the cortical tissue of $Nde1^{-/-}$ embryos compared to that of their WT littermates by IB analyses of cerebral cortical histone extracts. Notably, decreased H4K20me3 abundance was inversely correlated with the level of histone PTMs associated with mitosis (H3S10p) and DNA double-strand breaks (γH2A.X) in $Nde1^{-/-}$ cortices (Figure 2H), supporting the notion that DSBs and mitotic arrests in $Nde1^{-/-}$ NPCs result from aberrant heterochromatin replication and remodeling in neurogenic cell cycles. Taken together, our findings demonstrate that Nde1's essential role in neurogenesis involves effective epigenetic heterochromatin compaction, which is necessary for both patterning the chromatin landscape and for endowing genome stability of neocortical neurons. Considering the increasing demand on both epigenetic diversity and genome protection of neocortical neurons in mammalian evolution, this role of NDE1 should be more indispensable in humans than in mice.

NDE1/Nde1 is an IDP that can phase separate and bind to constitutive heterochromatin

To determine how NDE1 mediates heterochromatin remodeling and stability, we next investigated its molecular dynamics. At present, the mechanism that directs the *de novo* assembly of heterochromatin *in vivo* remains elusive, but recent work suggests that the formation of compact heterochromatin domains relies on the local accumulation of principle epigenetic heterochromatin writer molecules via a liquid-liquid phase separation (LLPS) (Larson et al., 2017; Strom et al., 2017). LLPS is generally believed to result from multivalent interactions between intrinsically disordered proteins (IDPs). This is well in line with the structure of NDE1, as both human and murine paralogs of NDE1/Nde1 contain an extended coiled-coil domain through which it can self-associate and/or mediate multiple molecular interactions in a concentration-dependent manner. Predictor of natural disordered regions (PONDR) also indicates that over 90% of NDE1/Nde1 protein is disordered, containing large intrinsically disordered regions (IDRs) (Figure 3A). This molecular feature also fully agrees with our previous data showing that Nde1 is a dynamic scaffold protein that can partition into various subcellular domains including the nucleus (Houlihan and Feng, 2014; Pawlisz and Feng, 2011). We thereby tested if NDE1/Nde1 can phase separate by expressing GFP-tagged Nde1 and evaluating its dynamic subcellular localization and biophysical properties in forming a condensed liquid state. We observed that GFP-Nde1 displayed a variety of patterns with respect to subcellular distribution. At higher concentrations, a majority of GFP-Nde1 formed membrane-less

condensates in both the cytoplasm and the nucleus (Figure 3B). These condensates exhibited liquid-like features, forming spherical droplets, showing rapid movement and exchange kinetics, and undergoing fusion to coalesce into larger spheres or immiscible compartments (Figure 3C–3F, Videos S1, S2, S3, and S4, fluorescence and phase contract live imaging of GFP-Nde1 dynamic movement and fusion events shown by Figures 3C and 3E, respectively). We monitored GFP-Nde1 turnover within droplets by fluorescence recovery after photobleaching (FRAP) and observed a quick recovery of both cytoplasmic and nuclear GFP-Nde1 after bleaching (Figures 3G and 3H). These dynamic cell molecular and biophysical properties enable NDE1/Nde1 to nucleate phase-separated compartments, making it an excellent candidate to facilitate the molecular assemblies necessary for heterochromatin condensation.

We next assessed the association of NDE1/Nde1 with heterochromatin in NPCs. In human neural stem/progenitor cultures, we found NDE1 localized predominantly in the nucleus and displayed a substantial co-localization with H4K20me3 modified chromatin (Figure 3I). Notably, NDE1-H4K20me3 co-localization is much stronger in densely packed than diffuse H4K20me3 domains, which supports a role of NDE1 in heterochromatin condensation. We further determined the physical interaction of Nde1 with heterochromatin. We have previously identified a direct interaction of Nde1 with the cohesin complex and showed that Nde1 LOF resembles the phenotypes of cohesinopathies (Houlihan and Feng, 2014). As the cohesin complex binds the pericentric heterochromatin with the highest affinity, we performed chromatin IP (ChIP) with antibodies against Nde1 and cohesion in parallel to assess whether Nde1 interacts with the centric- and pericentric-chromatin similarly as cohesin does in embryonic cortical tissue. As expected, both Nde1 and the Smc3 ChIP brought down pericentromeric major satellite and centromeric minor satellite repeats (Figure 3J). In comparison, the interaction of Nde1 with repetitive elements of LINE1 and IAP retroviral transposons, subtelomeres, and rDNA clusters was not robust and variable (Figure S3). This preferential interaction of Nde1 with satellite repeats further supports the involvement of Nde1 in the molecular assembly, compaction, and protection of centric and pericentric heterochromatin.

The nuclear partition of NDE1/Nde1 is directed by BRAP/Brap

The primary sequence of NDE1/Nde1 predicts a partial nuclear localization signal (NLS score of 5.8 by cNLS Mapper, and a score of 0.61 by NucPred). However, NDE1/Nde1 is efficiently targeted to the nucleus of NPCs to meet its functional demand in NPCs (Houlihan and Feng, 2014) (Figure 3I). We thus sought to determine the mechanism by which NDE1/Nde1 is directed to the nucleus. One of Nde1's essential molecular partner in CNS development is BRAP/Brap, a BRCA1 associated protein capable of interacting with the nuclear localization signals (NLS) through which it regulates the cytoplasmic retentions versus nuclear imports of its interacting molecules (Lanctot et al., 2013; Li et al., 1998). Nde1 and Brap both act in a dosage-sensitive manner and have common molecular interactors. We found the abundance and nuclear pool of Nde1 is maintained by Brap. In the developing cortical tissue of mice with Brap knockout ($Brap^{-/-}$) or Emx1-Cre-mediated Brap conditional knockout in dorsal telencephalic NPCs ($Brap^{flox/flox;Emx1Cre}$, referred to as $Brap^{cKO}$ hereafter), the level of Nde1 protein was substantially reduced than in WT and control mice (Figure 3K). Conversely, overexpressing recombinant Brap elevated not only Nde1's overall level but also Nde1's nuclear partition (Figures 3L–3N). These data suggested that whereas the stability of Nde1 relies on its interaction with Brap in the cytoplasm, Brap also promotes Nde1's nuclear targeting. Given that Brap can undergo autoubiquitination to up- and down-regulate its own levels in response to growth signals (Lanctot et al., 2013; Matheny et al., 2004), the unique characteristics of Brap are likely both necessary and sufficient for maintaining Nde1's abundance and directing Nde1's nuclear import in NPCs.

To ascertain that Brap is essential for Nde1's role in heterochromatin replication and remodeling during NPC differentiation, we determined whether Brap LOF phenocopies the heterochromatin defects of $Nde1^{-/-}$ in cortical NPCs. We have previously shown that $Brap^{-/-}$ NPCs have a shortened G1 phase but prolonged S phase in cell cycles toward neuronal differentiation, and that DNA replication in $Brap^{-/-}$ NPCs stalls in late S phase similar to $Nde1^{-/-}$ NPCs (Lanctot et al., 2017). To test whether the stalled DNA replication in $Brap^{-/-}$ NPCs phenocopied $Nde1^{-/-}$ NPCs with compromised H4K20me3, we analyzed the H4K20me3-dense foci and chromocenters in early, mid, late, and stalled S-phase NPCs identified by sequential IdU-CldU labeling (Figures S2A and S2B). As expected, we observed a significant decrease in the number of H4K20me3 foci in those $Brap^{-/-}$ NPCs that were in late S-phase or showed stalled DNA replication at heterochromatin domains (Figures S2A–S2D). Furthermore, the overall level of H4K20me3 is reduced in nascent cortical neurons of $Brap^{-/-}$ and $Brap^{cKO}$ embryos (Figures S2A, S2E, and S2F). This

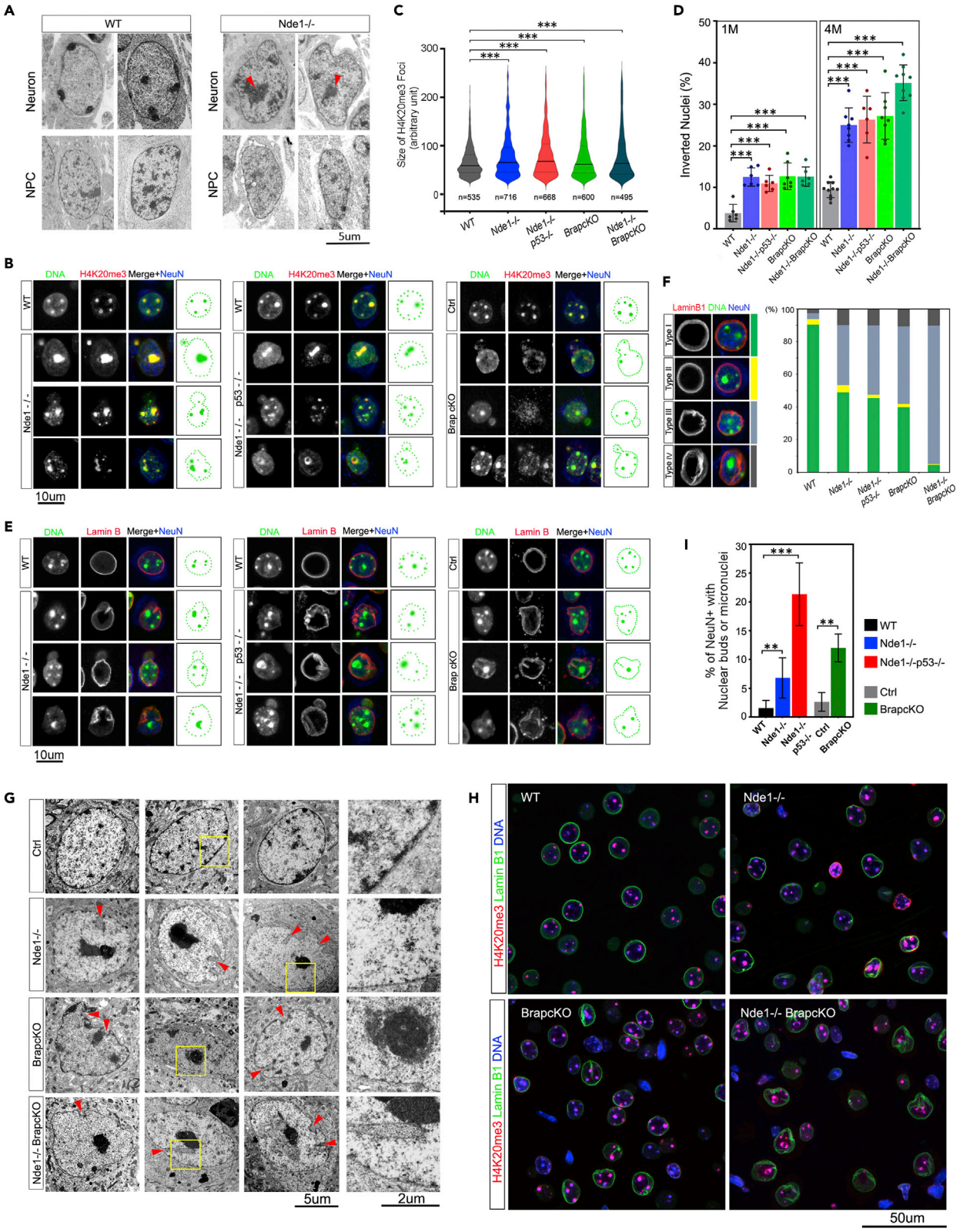
A
WT
Nde1-/-
Neuron
NPC
5um
C
Size of H4K20me3 Foci (arbitrary unit)
n=535
n=716
n=668
n=600
n=495
WT
Nde1-/-
Nde1-/- p53-/-
BrapcKO
Nde1-/- BrapcKO
D
1M
4M
Inverted Nuclei (%)
B
DNA H4K20me3 Merge+NeuN
Nde1 -/-
Nde1 -/- p53 -/-
Brap cKO
Ctrl
10um
F
LaminB1 DNA NeuN
Type I
Type II
Type III
Type IV
(%)
E
DNA Lamin B Merge+NeuN
I
% of NeuN+ with Nuclear buds or micronuclei
WT
Nde1-/-
Nde1-/-p53-/-
Ctrl
BrapcKO
G
Ctrl
Nde1-/-
BrapcKO
Nde1-/- BrapcKO
5um
2um
H
H4K20me3 Lamin B1 DNA
WT
Nde1-/-
BrapcKO
Nde1-/- BrapcKO
50um

Figure 4. Nde1 and Brap LOF result in nuclear architecture aberrations in heterochromatin-associated domains

(A) Transmission electron microscopy (TEM) images of representative cortical NPCs and neurons in WT or Nde1$^{-/-}$ embryos. Arrows indicate nuclear lamina aberrations. Bar: 5um.

(B) IH images of individual nuclei from cortical sections of mice at weaning age (P22-28), showing diverse nuclear architecture and heterochromatin (marked by H4K20me3) aberrations in cortical neurons (NeuN+) of WT, Nde1$^{-/-}$, Nde1$^{-/-}$p53$^{-/-}$, and Brap^{cKO} mice. Shown are representative images of nuclei from cortical sections of mice of indicated genotypes. n≥ 5 for each genotype. Bar:10um.

(C) Violin plots of H4K20me3 foci size distribution on IH images of cortical neurons in mice of genotypes indicated at weaning age (P22-P28). The total number of foci quantified (by Image-ProPremier) for each genotype is represented as median plus quartiles (n ≥ 3 mice per genotype). ***p<0.001 by two-sample Kolmogorov-Smirnov tests.

(D) Quantification of inverted nuclei (%) in cortical tissues of mice of genotype indicated at weaning (1M) and 4 months (4M) of ages. Shown are Mean ± SD and distributions of the percentage of inverted nuclei from different mice (n ≥ 3 mice per genotype). ***p<0.001 by student's t-tests.

(E) IH images of diverse nuclear architecture and nuclear lamina (marked by Lamin B1) in cortical neurons (NeuN+) of WT, Nde1$^{-/-}$, Nde1$^{-/-}$p53$^{-/-}$, and Brap^{cKO} mice at weaning age (P22-28). Shown are representative images of nuclei from cortical sections of mice of indicated genotypes (n ≥ 5 mice for each genotype). Bar:10um.

(F) Quantification of nuclear inversion, nuclear lamina aberration, and the coincidence of nuclear inversion and nuclear lamina aberration in neocortical neurons of mice of indicated genotypes at 3-4 months of age (data are represented as mean from n ≥ 3 mice for each genotype). The percentages of four types of nuclei were scored. Type I: conventional nuclei with normal nuclear lamina; Type II: inverted nuclei with normal nuclear lamina; Type III: conventional nuclei with aberrant nuclear lamina; Type IV: inverted nuclei with aberrant nuclear lamina.

(G) Transmission electron microscopy (TEM) images of representative nuclei of neocortical neurons of Nde1$^{-/-}$, Brap^{cKO}, Nde1$^{-/-}$Brap^{cKO}, and Control (Brap$^{flox/wt\ Cre-}$) adult mice (4-8 months of age). Arrows indicate nuclear lamina aberrations. Higher magnification images show decreased heterochromatin abundance at the nuclear periphery of mutant neurons. Bars: 5um or 2um as indicated.

(H) IH images of H4K20me3-Lamin B1 double stained neocortical sections of WT, Nde1$^{-/-}$, Brap^{cKO}, and Nde1$^{-/-}$Brap^{cKO} mice of weaning age (P22-P28). Note the phenocopy and synergy of Nde1 and Brap LOF. Bar: 50um.

(I) Frequency of nuclear buds or micronuclei in cortical neurons (NeuN+) of mice of genotypes indicated at weaning age (P22-P28). Mean ± SD, **p<0.01, ***p<0.001 by student's t-tests.DNA was visualized by staining with Hoechst 33,342. See also Figure S4.

phenotype in heterochromatin replication and H4K20me3 modification closely resembles what we observed in Nde1$^{-/-}$ NPCs. The phenocopy of Nde1 and Brap LOF strongly supports the functional collaboration between Brap and Nde1. Although BRAP/Brap plays a broader role than NDE1/Nde1 in regulating Ras signaling and ubiquitin-mediated protein turnover (Lanctot et al., 2013, 2017), Nde1 appears to be the key player downstream of Brap in heterochromatin establishment/compaction during cortical neurogenesis.

Heterochromatin and nuclear architecture aberrations in Nde1 and brap deficient neocortical neurons

As the epigenetic modification of constitutive heterochromatin is expected to be stably maintained, we asked whether the failures in H4K20me3 patterning that we observed in neurogenic Nde1$^{-/-}$ and Brap^{cKO} NPCs lead to chromatin defects of their daughter neurons. We first compared nuclei of newborn neurons in the cortical tissue of WT and Nde1$^{-/-}$ embryos by transmission electron microscope (TEM). We found that the most prominent gross defect displayed in some Nde1$^{-/-}$ neurons was an enlarged heterochromatin island in the center of the nuclei (Figure 4A). Heterochromatization typically drives the nuclear compartmentation by localizing euchromatin in the interior and heterochromatin at the periphery in conventional nuclei. By having a large heterochromatin condensate in the nuclear center but little or no heterochromatin in diverse nuclear domains and nuclear periphery, these Nde1$^{-/-}$ nuclei appear "inverted" with respect to chromatin compartments. Therefore, compromised heterochromatin replication and compaction in Nde1$^{-/-}$ NPCs may lead to nuclear architecture alterations in cortical neurons.

We further performed immunohistological (IH) analyses to determine the effect of Nde1 LOF on the nuclear architecture of mature neocortical neurons at post weaning ages. We included mice with Nde1 and Trp53 double LOF (Nde1$^{-/-}$p53$^{-/-}$) in order to rule out the effect of loss of NPCs or neurons because of Trp53-dependent apoptosis (Houlihan and Feng, 2014). In addition, Brap^{cKO} mice along with their control littermates (Brap$^{flox/+\ Cre-}$ or Ctrl) were analyzed in parallel to test whether Nde1 and Brap act in the same pathway of heterochromatin remodeling. A minimum of five mice of each genotype were analyzed using antibodies specific for heterochromatin and various nuclear landmarks. We first examined the size and distribution of heterochromatin condensates recognized by H4K20me3 immuno-signals. In most WT cortical neurons, H4K20me3 foci were relatively uniform in size and predominantly co-localized with the Hoechst-intense chromocenters (Figures 1E, 4B, and 4C). However, in Nde1$^{-/-}$, Nde1$^{-/-}$p53$^{-/-}$, and Brap^{cKO} cortical neurons, H4K20me3 foci exhibited a more heterogeneous pattern, showing a broader range in size and subnuclear distribution, with some congregated in the nuclear center and some dispersed

as speckles throughout the nucleus (Figures 4B and 4C). Coinciding with increased large H4K20me3 condensates, we observed a higher population of inverted nuclei in neocortical neurons of Nde1$^{-/-}$, Nde1$^{-/-}$p53$^{-/-}$, and Brap^{cKO} mice than in WT mice (Figure 4D). Although the fraction of inverted nuclei increased from weaning to adult ages in both WT and mutants, they remained significantly higher in mutants than in WT cortical tissues.

Inverted nuclei have been observed in retinal rod cells of nocturnal mammals and cells with lamin B receptor abrogation (Solovei et al., 2009, 2013). They are believed to result from loss of heterochromatin attractions to the nuclear lamina. Indeed, inverted nuclei that we observed in newborn neurons of Nde1$^{-/-}$ embryos displayed abnormal nuclear lamina, showing rumpled contour or invagination (Figure 4A arrows). Furthermore, we found inverted nuclei in mature neocortical neurons with Nde1 or Brap deficiency also coincided frequently with abnormal lamina revealed by lamin B1 immunoreactivities. Approximately half of the cortical neurons in Nde1$^{-/-}$, Nde1$^{-/-}$p53$^{-/-}$, and Brap^{cKO} mice displayed aberrant nuclear lamina, showing lobules and blebs or invaginations and crossed pieces because of loss of structure integrity or misplaced lamina that bisects the nucleus (Figures 4E and 4F). The heterochromatin and nuclear lamina aberration of mutant neocortical neurons were further revealed and confirmed by TEM, which showed that heterochromatin in the inverted nuclei of Nde1$^{-/-}$ and Brap^{cKO} neurons was largely absent from the nuclear lamina but tended to congregate near the nucleoli (Figure 4G). In parallel, the nucleoli in the mutant neocortical neurons also displayed higher heterogeneity in size relative to that of WT mice (Figure S4A). These data demonstrate that Nde1 and Brap LOF result in substantially altered chromatin compartmentation at a global nuclear level in neocortical neurons.

We also generated mice with Nde1 and Brap double LOF in neocortical tissues (Nde1$^{-/-}$Brap^{cKO}) and found that nuclear lamina were abnormal in nearly all cortical cells of the double mutant mice (Figures 4G and 4H). Likewise, phenotypes in H4K20me3 heterogeneity and nuclear inversion were significantly stronger in Nde1$^{-/-}$Brap^{cKO} double mutant mice than in mice with Nde1 and Brap single LOF (Figures 4D and4F). This furthersupports the functional synergy of Nde1 and Bap in heterochromatin compaction and stability.

We observed nuclear architecture aberrations in all cortical layers of Nde1$^{-/-}$ and Brap^{cKO} mice despite their preferential loss of layer II/III glutamatergic primordial neurons (Feng and Walsh, 2004; Lanctot et al., 2017). We also looked at GABAergic cortical interneurons that were generated in the ganglionic eminences of the ventral telencephalon and expressed parvalbumin (PV). Although the PV neurons in Nde1$^{-/-}$ cortices were not significantly decreased in number, they showed prevalent nuclear lamina aberrations (Figures S4C–S4E). Therefore, nuclear architecture defects can be a trait that dampens the quality and function of neocortical neurons independent of neurons' number and location.

Despite profound nuclear architecture aberrance of neocortical neurons, hippocampal neurons were mildly affected by Nde1 or Brap LOF (Figures S4F–S4H). As the neocortex is evolutionarily more recent than the hippocampus, the stronger neocortical phenotype in neuronal heterochromatin aberrance is in alignment with the higher indispensability of NDE1 in generating evolutionarily advanced neurons with greater demands in heterochromatin diversity and stability.

Consistent with a role of Nde1 and Brap in heterochromatin in maintaining genome stability, we detected nuclear buds and micronuclei in 10–20% of cortical neurons in Nde1$^{-/-}$, Nde1$^{-/-}$p53$^{-/-}$, and Brap^{cKO} mice. This was significantly higher compared to the only 1–4% found in WT or Ctrl cortices (Figure 4I). These gross nuclear anomalies are commonly associated with chromosomal fragmentation and mis-segregation. Therefore, our data together demonstrated that through proper heterochromatin establishment and/or maintenance, Nde1 and Brap are essential for protecting genome stability of neocortical neurons.

Nde1 LOF results in heterochromatin instability and DSBs in neocortical neurons

Proper chromatin organization has been demonstrated to have a striking effect on mutation rates, with rates being significantly higher in heterochromatin than in euchromatin (Roberts and Gordenin, 2014; Schuster-Bockler and Lehner, 2012). Therefore, heterochromatin aberrations in Nde1$^{-/-}$ and Brap^{cKO} neurons may be associated with heterochromatic DNA damage. To test this, we examined several markers for DSB in the cortical tissue of WT, Nde1$^{-/-}$, Nde1$^{-/-}$p53$^{-/-}$, and Brap^{cKO} mice. We have shown previously that γH2A.X, a hallmark for DSBs, peaked in Nde1$^{-/-}$ NPCs at the onset of neurogenesis but subsided in

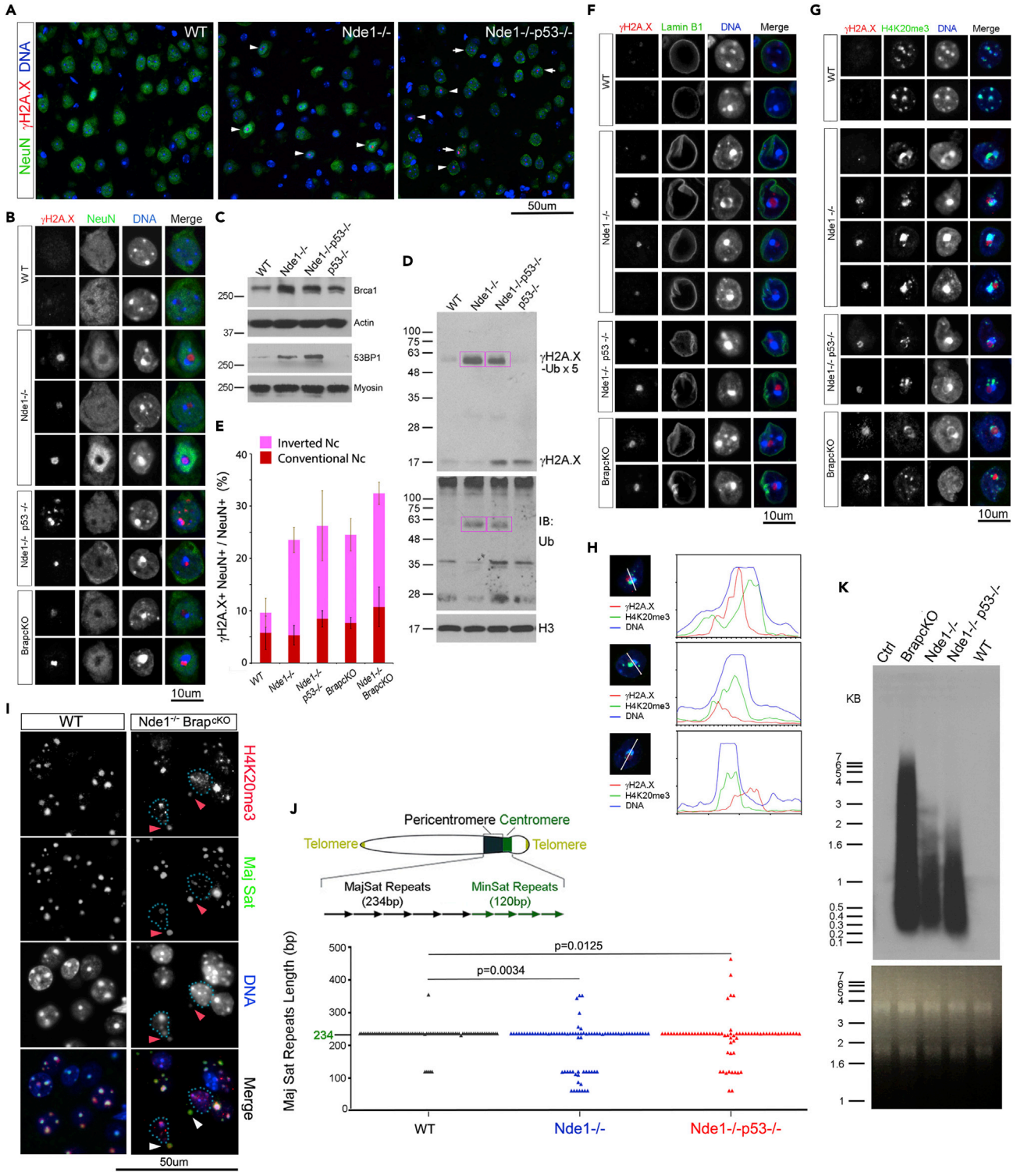

Figure 5. Nde1 and Brap LOF results in heterochromatin DSBs and increased transcription of pericentromeric satellite repeats

(A and B) Representative IH images of γH2A.X-NeuN double immuno-labeled neocortical sections of 4 monthold WT, Nde1$^{-/-}$, and Nde1$^{-/-}$p53$^{-/-}$ mice. Note that γH2A.X is shown specifically in the nucleus of NeuN+ cells (arrow heads). Bars: 50um or 10um asindicated.

(C) IB of total cortical protein extracts from 4 month old mice of indicated genotypes. Note the substantial elevation of Brca1 and 53BP1 in Nde1$^{-/-}$ and Nde1$^{-/-}$p53$^{-/-}$ cortical tissues.

Figure 5. *Continued*

(D) IBs of histone extracts with anti-γH2A.X (upper image) and anti-ubiquitin (lower image) antibodies, showing increased γH2A.X (~17kDa) and penta-ubiquitinated γH2A.X (boxed, ~60 kDa) in cortical tissues of Nde1$^{-/-}$ and Nde1$^{-/-}$p53$^{-/-}$ mice of 4 months of age. The blot was re-probed with an anti-ubiquitin antibody after stripping off γH2A.X signals, confirming that the higher molecular weight band of ~60 kDa recognized by anti-γH2A.X (boxed) contains ubiquitin modification. Loading was normalized to histone H3.

(E) Quantification (%) of neurons (NeuN+) showing γH2A.X and inverted nuclei in cortical tissue of 4 monthsold mice of genotypes indicated. Mean ± SD, *p< 0.001 by student's t tests.

(F) Representative IH images of selected nuclei in γH2A.X-LaminB1 double immune-labeled neocortical neurons in adult (3-4 months old) WT, Nde1$^{-/-}$, Nde1$^{-/-}$p53$^{-/-}$, and Brap^{cKO} mice. Note the coincidence of large γH2A.X foci in neurons with aberrant nuclear lamina. Bar: 10um.

(G) Representative IH images of selected nuclei in γH2A.X-H4K20me3 double immuno-labeled neocortical neurons in adult (3-4 month old) WT, Nde1$^{-/-}$, Nde1$^{-/-}$p53$^{-/-}$, and Brap^{cKO} mice. Bar: 10um.

(H) Representative line scans of γH2A.X, H4K20me3, and Hoechst 33,342 fluorescence intensities of selected individual nuclei, revealing the spatial proximity of γH2A.X with heterochromatin condensates.

(I) Immuno-FISH analysis with a probe for major satellite DNA (green) and an antibody to H4K20me3 (red) on mouse neocortical sections. Shown are representative images, demonstrating the presence of pericentromeric major satellite repeats in the micronuclei of Nde1-Brap double deficient neocortical cells. Note the weaker H4K20me3 in the micronuclei (arrows). Bar: 50um.

(J) PCR, cloning, and sequencing analyses of adult (2-4 months) cerebral cortical genomic DNA, showing increased polymorphic length variations of pericentromeric major satellite repeats in Nde1$^{-/-}$, Nde1$^{-/-}$p53$^{-/-}$ cortices. Data were from n ≥ 3 mice per genotype. A total of 100 PCR clones were sequenced from each genotype. Data present all clones containing PCR inserts with MajSat sequences. p values by two-sample Kolmogorov-Smirnov tests are indicated.

(K) Northern blot analysis of pericentromeric major satellite RNA in cerebral cortical tissues of 8–10 months old mice of indicated genotypes. The integrity and the amount of RNA loaded are shown by ethidium bromide stained gel below. See also Table S1. Major satellite length distribution.

later embryonic and early postnatal periods (Houlihan and Feng, 2014). However, after the mutant mice aged to 3 months or older, we found γH2A.X became readily detectable again in the cortical tissue of Nde1$^{-/-}$, Nde1$^{-/-}$p53$^{-/-}$, and Brap^{cKO} mice. Notably, γH2A.X immunosignals were found predominantly in neurons (NeuN+) but rarely in glia (NeuN-) (Figures 5A and 5B). Consistent with the presence of γH2A.X, 53BP1 and Brca1, the two essential molecules for DSB repair, were also upregulated in Nde1$^{-/-}$ and Nde1$^{-/-}$p53$^{-/-}$ compared to WT and p53$^{-/-}$ cortical tissues (Figure 5C). Moreover, IB of cortical histone extracts not only confirmed the elevation of γH2A.X in the cortical tissue of Nde1$^{-/-}$ and Nde1$^{-/-}$p53$^{-/-}$ mice but also showed that the increased γH2A.X in Nde1$^{-/-}$ and Nde1$^{-/-}$p53$^{-/-}$ mice were predominantly penta-ubiquitinated (Figure 5D, boxed bands). The dual PTM of phosphorylation and ubiquitination of histone H2A.X is a characteristic DNA damage response that we observed in Brap^{cKO} mice and postmortem brains of patients with Alzheimer's disease (Guo et al., 2021). Therefore, heterochromatin aberrations resulting from Nde1 LOF can lead to genome instability and DSBs in adult cortical neurons with age-dependent progression and pathological impacts.

Further supporting a direct link between DSBs and abnormal chromatin structure in the mutant neurons, we found that more than 60% of cortical neurons that exhibited γH2A.X immunoreactivities also presented inverted nuclei (Figure 5E). In the cortical tissue of Nde1$^{-/-}$, Nde1$^{-/-}$p53$^{-/-}$, and Brap^{cKO} mice, DSBs were prevalently detected in nuclei that exhibited severe nuclear lamina and heterochromatin aberrations (Figures 5F and 5G). In these nuclei, γH2A.X foci were found almost exclusively embedded in or flanking the heterochromatin condensates labeled by H4K20me3 and Hoechst-intense chromocenters (Figures 5G and 5H). This spatial proximity of DSBs with H4K20me3 condensates agrees with previous observations that DSBs are corralled to heterochromatin to increase protection against nuclease degradation of open chromatin ends and to facilitate homologous recombination (HR)-mediated repair (Ayoub et al., 2008; Ryu et al., 2015). Alternatively, this is also likely to indicate that DSBs occurred in heterochromatin DNA in mutant neurons because the phosphorylation event resulting in γH2A.X can spread over hundreds of thousands to millions of bases (Gatti et al., 2012). To ascertain that the nuclear aberration indeed involves the physical damage of constitutive heterochromatin in Nde1$^{-/-}$ and Brap^{cKO} neurons, we performed immunoFISH analysis using a probe for pericentromeric major satellite repeats (MajSat). We found that MajSat DNA was present in extranuclear micronuclei of Nde1$^{-/-}$Brap^{cKO} double mutant cortical neurons, and that some micronuclei showed reduced H4K20me3 immunoreactivity (Figure 5I, arrows). Therefore, DSBs and chromatin fragmentations can occur in the satellite repeats because of Nde1 and Brap deficiency. These results also suggested that compromised H4K20me3 led to gross chromosomal breaks and rearrangements.

To further determine the impact of aberrant H4K20me3 and heterochromatin compaction on heterochromatin integrity, we asked whether Nde1 LOF results in changes in DNA sequence of heterochromatic

repeats because chromatin compaction by H4K20me3 prevents unscheduled homologous recombination of the underlying repetitive DNA (Bierhoff et al., 2014; Marion et al., 2009; Schotta et al., 2008; Wongtawan et al., 2011). In mice, the pericentromeric heterochromatin consists of large uninterrupted arrays of AT-rich major satellite repeats 234 base pairs in length that can extend more than 2 megabases per chromosome (Vissel and Choo, 1989). Because these extremely long repetitive DNA sequences are difficult to assess by Next Generation Sequencing, we used a PCR-based strategy to amplify MajSat monomers, cloned the PCR products, and sequenced each individual PCR clone by Sanger sequencing. Data of genomic DNA isolated from cortical tissues of adult WT, Nde1$^{-/-}$, and Nde1$^{-/-}$p53$^{-/-}$ mice at 2–4 months of age were analyzed. We found 90% of the WT clones contained the standard monomers of MajSat repeats (75 of 83 clones from four mice), but only 55% of Nde1$^{-/-}$ clones (46 of 83 clones from four mice) and 57% of Nde1$^{-/-}$p53$^{-/-}$ clones (40 of 70 clones from three mice) contained canonical MajSat monomers of 234 base pairs. The rest of the clones showed irregular length, which indicated that Nde1 LOF resulted in alterations in the sequence and structure of MajSat repeats (Figure 5J, Table S1, Major satellite length distribution). Such variants in MajSat sequence support the notion that failures in heterochromatin compaction can lead to instability and undesired recombination of repetitive DNA elements in Nde1 deficient cortical tissues.

High MajSat transcription from heterochromatin derepression in Nde1$^{-/-}$cortical tissue

Heterochromatin compaction is a key mechanism for repressing the transcription of its underlying repetitive DNA sequences to maintain their stability. The sequence irregularity of MajSat repeats and the presence of MajSat DNA in micronuclei suggested compromised compaction and silencing of the MajSat repeats in Nde1$^{-/-}$ cortices. We thus tested whether the structure aberrance and DSBs of heterochromatic DNA in Nde1$^{-/-}$ cortices were associated with the derepression of satellite transcription. By northern blotting analysis, we detected high levels of major satellite-derived transcripts in Nde1$^{-/-}$, Nde1$^{-/-}$p53$^{-/-}$, and Brap^{cKO} cortical tissue (Figure 5K). These transcripts ranged from 200 to 6 kilobases, which was reminiscent of the aberrant over-expression of satellite repeats in mouse pancreatic ductal adenocarcinomas (Ting et al., 2011). As MajSat RNA transcripts were shown to be enriched in BRCA1 deficient breast cancers and acted as potent inducers of DNA damage (Zhu et al., 2018), the accumulation of pericentromeric satellite transcripts may account for DSBs and heterochromatin fragmentations in Nde1 and Brap deficient neurons.

Progeria-like histone PTMs, neuroinflammation, and neurodegeneration in Nde1$^{-/-}$brains

The heterochromatin aberrations that we observed in the Nde1$^{-/-}$ cortical tissue were reminiscent of the chromatin signatures of cancer and progeroid syndromes. However, there were no tumor-like phenotypes in the brain of Nde1$^{-/-}$ and Nde1$^{-/-}$p53$^{-/-}$ mice, though some mutant mice that died between 3 and 12 months showed tumors outside of the CNS. This suggested that the consequence of DSBs and heterochromatin aberration in post-mitotic neurons is premature aging. This is supported by our study of Brap^{cKO} mice, which revealed a significant lifespan shortening along with accelerated cellular senescence and neurodegeneration (Guo et al., 2021). Therefore, we tested whether Nde1 LOF shared the characteristic histone PTMs of premature aging in progeroid syndromes. Hutchinson-Gilford Progeria syndrome (HGPS) is caused by *LMNA* mutations that affect lamin A processing. The aberrant lamin A proteins destabilize nuclear lamina and result in DSB accumulation similar to what we observed in Nde1 and Brap deficient cortical neurons (Liu et al., 2006; Scaffidi and Misteli, 2005). The nuclear and chromatin defects of HGPS are characterized by H4K20me3 upregulation (Arancio et al., 2014; Shumaker et al., 2005), whereas loss of H4K20me3 is a hallmark of cancer (Fraga et al., 2005; Yokoyama et al., 2014). Similarly, despite an initial H4K20me3 reduction in the developing cortices (Figures 2H and S2F), Nde1$^{-/-}$ and Brap^{cKO} mice showed higher levels of H4K20me3 in the adult and aging cortical tissue compared with their WT or control counterparts (Figure 6A). This age-dependent H4K20me3 upregulation in Nde1$^{-/-}$ and Brap^{cKO} mice resembled the histone PTM changes of HGPS. It is also likely associated with cellular senescence (Nelson et al., 2016) and/or acts as a compensatory response to suppress the recombination and breaking of satellite repeats.

The progeria-like H4K20me3 elevation in Nde1$^{-/-}$ cortical tissue also coincided with increased histone H2A ubiquitination (H2Aub) (Figure 6A), a histone PTM that can occur on multiple sites of H2A in a context dependent manner to mediate transcriptional suppression and/or DNA repair (Uckelmann and Sixma, 2017). Ubiquitination on K119 by Polycomb repression complex 1 (PRC1), known to promote chromatin compaction and transcriptional silencing, was also reported to be a conserved biomarker for aging (Yang et al., 2019). Our data showed that histone H2Aub is a hallmark phenotype of Brap LOF and a pivotal

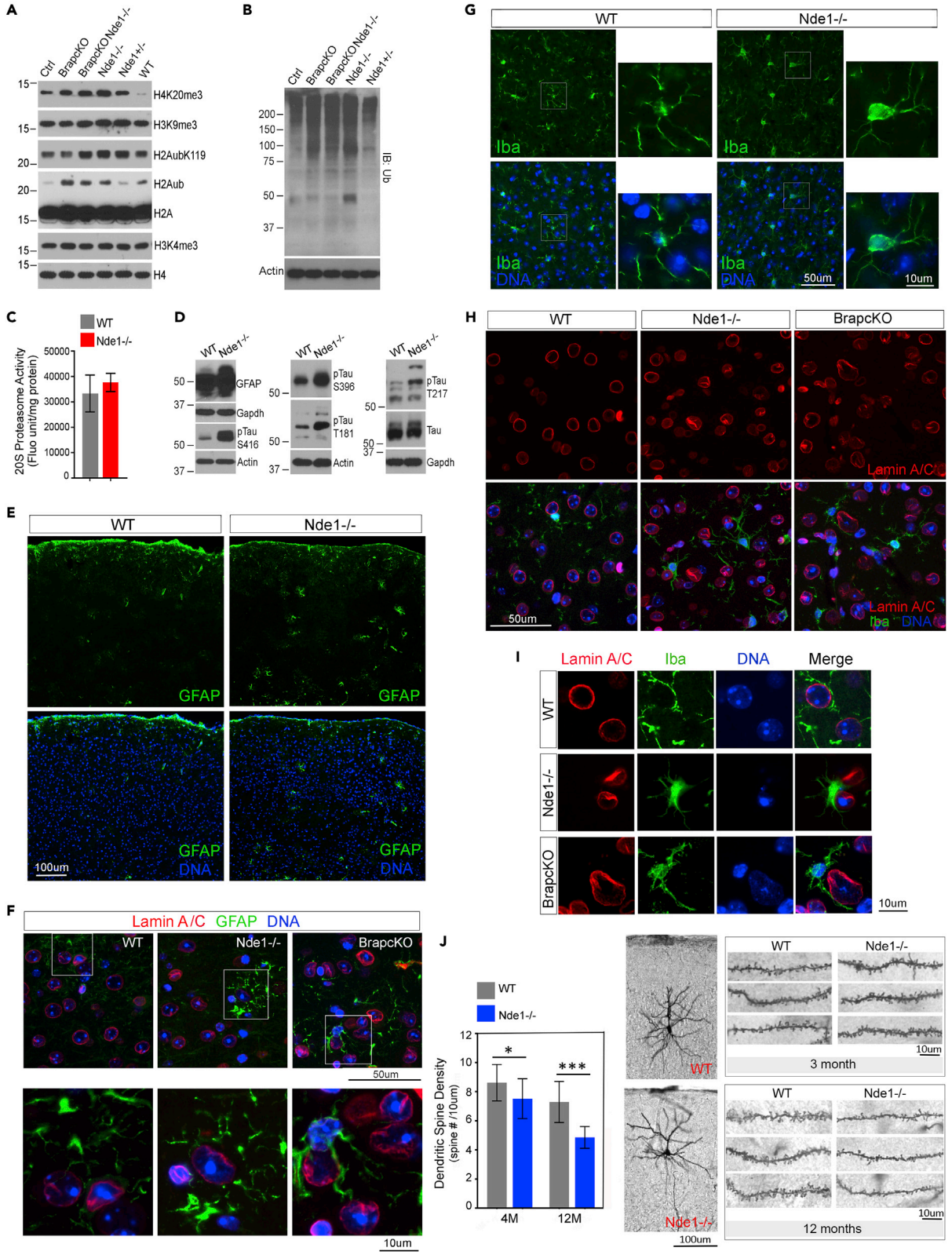
A
Ctrl
BrapcKO
BrapcKONde1-/-
Nde1-/-
Nde1+/-
WT
H4K20me3
H3K9me3
H2AubK119
H2Aub
H2A
H3K4me3
H4
B
IB: Ub
Actin
C
WT
Nde1-/-
20S Proteasome Activity (Fluo unit/mg protein)
D
GFAP
Gapdh
pTau S416
pTau S396
pTau T181
pTau T217
Tau
Actin
E
WT
Nde1-/-
GFAP
GFAP DNA
100um
F
Lamin A/C GFAP DNA
WT
Nde1-/-
BrapcKO
50um
10um
G
WT
Nde1-/-
Iba
Iba DNA
50um
10um
H
WT
Nde1-/-
BrapcKO
Lamin A/C
Lamin A/C Iba DNA
50um
I
Lamin A/C
Iba
DNA
Merge
WT
Nde1-/-
BrapcKO
10um
J
WT
Nde1-/-
Dendritic Spine Density (spine # /10um)
*
***
4M
12M
WT
Nde1-/-
100um
3 month
12 months
10um

Figure 6. Nde1 LOF induces progeria and aging associated histone PTMs, neuroinflammation, and neurodegeneration

(A) IB of histone extracts from cortical tissues of mice of indicated genotypes at 4 months of age. Shown are representative images. Note the substantial increase in H4K20me3 and H2Aub in the cortical tissues with Nde1 or Brap LOF.

(B) Ubiquitin IBs of cortical tissue total protein extracts from mice of indicated genotypes at 4 months of age. Note the accumulation of poly-ubiquitinated proteins in the cortical tissues with Nde1 or Brap LOF.

(C) Proteasome activity analysis of WT and Nde1$^{-/-}$ cortical tissues. Samples were prepared from 8-10 monthold WT and Nde1$^{-/-}$ mice. 20S proteasome activity (mean ± SD) was determined by assessing the amount of Suc-LLVY-AMC cleavage.

(D) IB of cortical tissue total protein extracts from mice of indicated genotypes at 10 months of age. Shown are representative images. Note the increased levels of GFAP and phospho-tau in Nde1$^{-/-}$ compared to WT mice.

(E) IH images of GFAP (green) labeled cortical sections of WT and Nde1$^{-/-}$ mice at 12 months of age. Shown are representative images. Note the increased and enlarged GFAP+ cells in Nde1$^{-/-}$ mice compared to their WT littermates. Bar: 100um.

(F) IH images of GFAP (green)-Lamin A/C (red) double immuno-labeled cortical sections of mice of indicated genotypes at 6 months of age. Shown are representative images. High-magnification views of the boxed areas are included. Note the spatial coincidence of aberrant nuclei and reactive astrocytes. Bars: 50um or 10um as indicated.

(G) IH images of Iba (green) labeled cortical sections of WT and Nde1$^{-/-}$ mice at 12 months of age. Shown are representative images. High-magnification views of the boxed areas are included. Note the morphological difference of microglia between WT and Nde1$^{-/-}$ mice. Bars: 50um or 10um as indicated.

(H) IH images of Iba (green)-Lamin A/C (red) double immuno-labeled mouse cortical sections of indicated genotypes at 6 months of age. Note the spatial coincidence of aberrant nuclei and activated microglia with ameboid morphology. Bar: 50um.

(I) High-magnification views of aberrant nuclei (marked by Lamin A/C, red) embraced by activated microglia (Iba, green). Bar: 10um.

(J) Quantification of dendritic spine density (Mean ± SD) and representative images of Golgi-cox analyses of WT and Nde1$^{-/-}$ mice at 3 and 12 months of age, showing age-dependent reduction in spine density in cortical layer $^{2}/_{3}$ pyramidal neurons of Nde1$^{-/-}$ mice. *p<0.01, ***p<0.0001 by Student's t tests. Bars: 100um or 10um as indicated.Nuclear DNA was stained with Hoechst 33,342 in blue in all IH images.

mechanism to promote neurodegeneration by inducing histone degradation, proteasome overflow, and leading to a backlog of poly-ubiquitinated proteins in the cortical tissue(Guo et al., 2021). In the cortical tissue of Nde1$^{-/-}$ mice whereas a change in H2Aub was not evident during embryonic and neonatal development, H2Aub was significantly elevated along with penta-ubiquitinated γH2A.X at ages of 3–4 months or older (Figures 6A and 5E). As both H4K20me3 and H2Aub are histone PTMs that promote heterochromatin compaction, their spatiotemporal coincidence with elevated γH2A.X and nuclear architecture aberrations in aging Nde1$^{-/-}$ and Brap^{cKO} neurons likely reflect compensatory heterochromatin remodeling to cope with recurrent DSBs in the repetitive DNA. However, such histone PTMs may also induce secondary epigenetic and proteomic alterations, leading to premature brain aging as observed in Brap^{cKO} mice(Guo et al., 2021).

To corroborate that the heterochromatin defects in Nde1$^{-/-}$ neurons can prime premature brain aging, we examined several phenotypes associated with neurodegeneration. Similar to what we found in Brap^{cKO} mice, the high histone H2Aub in the cortical tissue of Nde1$^{-/-}$ mice coincided with a buildup of poly-ubiquitinated proteins at ages older than eight to ten months, even though the proteasome activates remained unaltered (Figures 6B and 6C). Also resembling what we observed in Brap^{cKO} mice, the proteomic aberrance in Nde1$^{-/-}$ cortical tissues was accompanied by astrogliosis, microgliosis, and hyper-phosphorylation of the microtubule-associated protein tau, which are all brain pathology hallmarks in the preclinical stage of neurodegenerative diseases (Figures 6D–6I). We found that Glial Fibrillary Acidic Protein (GFAP), of which upregulation is a marker of reactive astrogliosis, was higher in the neocortices of Nde1$^{-/-}$ mice compared to their WT littermates (Figures 6D–6F). We also examined microglia, the resident immune cells of the brain. In WT cortical tissues, most microglia, identified by Iba, showed a ramified resting state appearance with many thin processes extending from a small cell body (Figure 6G). In contrast, many microglia in Nde1$^{-/-}$ cortices exhibited an ameboid shape with enlarged cell body and thicker processes (Figure 6G–6I). These morphology characteristics indicated that microglia in Nde1$^{-/-}$ cortical tissue were induced to enter a highly active state by pathological lesions. Notably, we found that the reactive astrocytes and microglia surrounded or closely contacted those neurons with severe nuclear lamina aberrations (Figures 6F, 6H, and 6I). These suggest that astrogliosis and microgliosis in Nde1$^{-/-}$ neocortical tissue were induced by the abnormal build-up of polyubiquitinated proteins and their associated toxic metabolites resulting from chromatin impairments and DNA damage responses.

To ascertain that the combined defects, including heterochromatin instability, the backlog of polyubiquitinated proteins, tau hyper-phosphorylation, and neuroinflammation, together promoted neurodegeneration, we examined the dendritic spines of neocortical neurons in aged Nde1$^{-/-}$ mice because dendritic spine dysfunction is considered critical for the pathogenesis of neurodegenerative diseases and highly correlated with cognitive decline of Alzheimer's disease. We performed Golgi-Cox staining to visualize

the morphology and dendritic spines of neocortical layer II/III pyramidal excitatory neurons in WT and Nde1$^{-/-}$ mice. Although the gross morphology and dendritic branching pattern were not obviously affected by Nde1 LOF, the density of dendritic spines in Nde1$^{-/-}$ neurons were significantly decreased compared to that in WT neurons (Figure 6J). This reduction in spine density was relatively mild at 4 months but became substantial as Nde1$^{-/-}$ mice further aged to 12 months (Figure 6J). The layer II/III pyramidal excitatory neurons of the neocortex are essential for neuronal networking across various cortical regions and between the two cerebral hemispheres. Loss of dendritic spines in these neurons would impair their synaptic transmission and compromise higher-order brain functions. Given that neurons of neocortical layer II/III largely account for the microcephaly phenotype of Nde1$^{-/-}$ mice, progressive functional decline of these neurons during adulthood would further drive cognitive decline and accelerate neurodegeneration in the mutant mice.

DISCUSSION

The neocortex is the structure responsible for all higher-order brain functions, and neurons in the neocortex represent the largest repertoire of cell number, diversity, and functional complexity across all tissues. These cells cease dividing at birth but function constantly with respect to electrical and metabolic activities throughout the organism's lifespan. These distinctive features make it both an extraordinarily essential and a daunting task to ensure the number, diversity, and genome stability in neocortical neurons. What we learned through studying the function of NDE1/Nde1 illuminates a mechanism by which the diversity and stability in these cells may be co-established through heterochromatin condensation. Although neurons in the brain can be classified by various subtypes based on their morphology, location, neurotransmitters, gene expression profiles, and neurocircuitry, recent work integrating spatial genomics with super-resolution imaging of RNA and epigenetic markers has demonstrated that the nine major types of cells within the murine cerebral cortex each have distinct nuclear features and cell type-specific chromatin architecture related to their differential transcriptional states (Takei et al., 2021). Therefore, the result of our study aligns well with these new multimodal genomics findings. Our data further contribute to this emerging concept on a relationship between epigenetic landscape and cell type diversity by suggesting that differential heterochromatin compaction during neurogenesis may further increase the heterogeneity of nuclear architecture. Thus, variations in heterochromatin landscapes may possibly not only add a new dimension to neurons' epigenetic diversity, but also fine-tune gene expression, modulate synaptic connection, regulate network activities, and enhance the fitness against genotoxic insults.

Importantly, our data not only show heterochromatin establishment is critical during neurogenesis, but also suggest that Nde1 is an essential player for both neocortical neurogenesis and heterochromatin patterning by H4K20me3, a PTM that is not only abruptly elevated in neurogenesis but also diversely distributed throughout neuronal populations in the cerebral cortex. Nde1 LOF compromises H4K20me3 and results in intractable DSBs in neocortical neurons. Of special interest is the pericentromeric MajSat repetitive elements regulated by Nde1. These satellite repeats are modified by H4K20me3, assemble into highly condensed constitutive heterochromatin, and remain permanently condensed during interphase of most somatic cells. This is essential to ensure the structural integrity and transcriptional silencing of these highly repetitive yet important genomic regions. It is known that the pericentric repetitive sequences flank the centromeres and are bound by cohesin, playing a major role in maintaining sister chromatid cohesion around centromeres to prevent premature chromatid separation during mitosis (Bernard, Science, 2001). We now demonstrate that these elements are protected additionally by the cohesin binding protein Nde1. Concomitantly, Nde1 also controls the epigenetic silencing and condensation of these repetitive elements to stabilize the heterogeneous chromatin landscapes in post-mitotic neocortical neurons. Therefore, the indispensable role of NDE1/Nde1 in neocortical development is to ensure the epigenetic remodeling and stability of pericentromeric constitutive heterochromatin and its underlying satellite repeats.

Satellite DNA sequences are the most dynamic element of genome evolution, presenting specific sequences and distribution patterns that are associated with polygenesis and species-identities (Thakur et al., 2021). However, the role of satellite repeats and their associated constitutive heterochromatin remains unclear, as their high repetitiveness makes them almost entirely missing from the genome assembly in the past two decades, and a lack of *in vivo* models to determine their functional impacts also hinders their study. Recent advances in fully sequencing the T2T-CHM13 genome now demonstrate the rich genetic and epigenetic variations hidden in the repeat elements of the human genome (Nurk et al., 2022;Altemose

et al., 2022; Gershman et al., 2022; Hoyt et al., 2022;Aganezov et al., 2022). Our finding of hyper-variability of heterochromatin landscape in human neocortical neurons as well as their physical and functional regulation by NDE1/Nde1 aligns fully with the new human genome information. Results of this study also illuminate the possible role of satellite repeats in evolutionarily-mediated control of neocortical neuronal identity, diversity, and genome stability. Therefore, the increased chromatin complexity and epigenetic diversity impose a stronger demand on NDE1, making it more indispensable in humans than in mice.

Our finding provides critical insight into a potential mechanism underlying the common etiology of neurological and psychiatric disorders. Neuropsychiatric illnesses, such as schizophrenia, depression, autism, ADHD, and epilepsy, are diagnosed based on their clinical presentations rather than molecular biomarkers. However, with respect to clinical manifestation, each of these disorders presents highly heterogeneous symptoms. Conversely, many of these disorders share common symptoms and/or often demonstrate comorbidity with each other. Moreover, the clinical symptoms of neuropsychiatric disorders are also observed in neurodegeneration. As a matter of fact, patients with neurodegenerative disorders not only exhibit social behavioral deficits, but the neuropsychiatric symptoms are even considered relevant indexes for determination of the severity and progression of neurodegeneration. Although the complex traits of neuropsychiatric and neurodegenerative disorders are believed to result from multiple genetic determinants and their interaction with environmental factors, mutations of genes controlling the genome stability and epigenetic regulation can result in somatic chromatin aberrations and/or DSBs in various neurons and brain regions. Given the stochastic nature of somatic genetic and epigenetic alterations, heterogeneous clinical phenotypes are expected. This explains how aberrations in a single gene, NDE1, can give rise to multiple brain disorders with a wide spectrum of clinical symptoms but without necessarily reducing the number of neocortical neurons. In addition, as NDE1 is a scaffold IDP that enables it to undergo multivalent interactions through LLPS, it can form biomolecular condensates encompassing multiple proteins and genomic regions. Therefore, either an increase or decrease in the abundance of NDE1 is expected to alter NDE1-dependent molecular condensates, causing substantial change in diverse cellular activities. Indeed, the dynamic phase separation properties of NDE1 offer a plausible mechanistic basis for clinical observations of overlapping, yet diverse, neuropsychiatric syndromes with copy number variations caused by both microdeletion and microduplication of NDE1 in 16p13.11.

Limitation of the study

Although data presented by this study demonstrate the essential contribution of NDE1/Nde1 in regulating heterochromatin compaction, stability, and histone H4K20 trimethylation, the mechanism by which Nde1 mediates these epigenetic changes remains elusive. The study is limited by the heterogeneity of the neocortical tissue and technical challenges in analyzing repetitive sequences of the genome. Further in-depth analyses of Nde1's interaction and coordination with heterochromatin writers and readers in various brain regions, neuronal subtypes, and ages are necessary. In addition, recent advances in sequencing repetitive regions of the genome, which were not available at the time of this study, will allow the more detailed analyses in the future.

STAR★METHODS

Detailed methods are provided in the online version of this paper and include the following:

- KEY RESOURCES TABLE
- RESOURCE AVAILABILITY
  - Lead contact
  - Materials availability
  - Data and code availability
- EXPERIMENTAL MODEL AND SUBJECT DETAILS
  - Mice
  - Human cerebral cortical tissue samples
  - Cell culture
- METHOD DETAILS
  - Cell culture, transfection, and fluorescence microscopy
  - Time-lapse fluorescence microscopy
  - Fluorescence recovery after photo-bleaching (FRAP)
  - Immunoblotting

- Histone extractions
- Immunohistological analyses
- Ultra-structural analysis
- Golgi-cox staining and dendritic spine analysis
- Nucleotide administration and S-phase analysis
- Chromatin immunoprecipitation
- Northern blot analysis
- Mouse major satellite genomic DNA analysis
- ImmunoFISH analysis
- 20S proteasome assay

● QUANTIFICATION AND STATISTICAL ANALYSIS

SUPPLEMENTAL INFORMATION

Supplemental information can be found online at https://doi.org/10.1016/j.isci.2022.104354.

ACKNOWLEDGMENTS

The authors wish to thank Sui Huang of Northwestern University for providing antibodies and for discussion. This work was supported by R01HD56380 and startup funds of Northwestern University and Uniformed Services University of the Health Sciences to Y.F.

Disclaimer: The opinions, interpretations, conclusions and recommendation are those of the authors and are not necessarily endorsed by the U.S. Army, Department of Defense, the U.S. Government or the Uniformed Services University of the Health Sciences. The use of trade names does not constitute an official endorsement or approval of the use of reagents or commercial hardware or software. This document may not be cited for purposes of advertisement.

AUTHOR CONTRIBUTIONS

Y. F conceptualized the project, designed and performed the experiments, interpreted the results, and wrote the manuscript. A.A.C designed and performed the experiments, interpreted the results, and wrote the manuscript; C.C.L performed experiments; Y.G. performed experiments; C.K. performed the experiments; D.M. performed cell imaging and FRAP analyses; H.P performed experiments; Q.Z. performed experiments; X.Z assisted with experiments; M.L.D assisted with experiments.

DECLARATION OF INTERESTS

The authors declare that they have no conflict of interest.

Received: October 5, 2021
Revised: March 28, 2022
Accepted: April 29, 2022
Published: June 17, 2022

REFERENCES

Aganezov, S., Yan, S.M., Soto, D.C., Kirsche, M., Zarate, S., Avdeyev, P., Taylor, D.J., Shafin, K., Shumate, A., Xiao, C., et al. (2022). A complete reference genome improves analysis of human genetic variation. Science *376*, eabl3533. https://doi.org/10.1126/science.abl3533.

Alkuraya, F.S., Cai, X., Emery, C., Mochida, G.H., Al-Dosari, M.S., Felie, J.M., Hill, R.S., Barry, B.J., Partlow, J.N., Gascon, G.G., et al. (2011). Human mutations in NDE1 cause extreme microcephaly with lissencephaly. Am. J. Hum. Genet. *88*, 536–547. https://doi.org/10.1016/j.ajhg.2011.04.003.

Allach El Khattabi, L., Heide, S., Caberg, J.H., Andrieux, J., Doco Fenzy, M., Vincent-Delorme, C., Callier, P., Chantot-Bastaraud, S., Afenjar, A., Boute-Benejean, O., et al. (2020). 16p13.11 microduplication in 45 new patients: refined clinical significance and genotype-phenotype correlations. J. Med. Genet. *57*, 301–307. https://doi.org/10.1136/jmedgenet-2018-105389.

Allshire, R.C., and Madhani, H.D. (2018). Ten principles of heterochromatin formation and function. Nat. Rev. Mol. Cell Biol. *19*, 229–244. https://doi.org/10.1038/nrm.2017.119.

Altemose, N., Logsdon, G.A., Bzikadze, A.V., Sidhwani, P., Langley, S.A., Caldas, G.V., Hoyt, S.J., Uralsky, L., Ryabov, F.D., Shew, C.J., et al. (2022). Complete genomic and epigenetic maps of human centromeres. Science *376*, eabl4178. https://doi.org/10.1126/science.abl4178.

Arancio, W., Pizzolanti, G., Genovese, S.I., Pitrone, M., and Giordano, C. (2014). Epigenetic involvement in Hutchinson-Gilford progeria syndrome: a mini-review. Gerontology *60*, 197–203. https://doi.org/10.1159/000357206.

Ayoub, N., Jeyasekharan, A.D., Bernal, J.A., and Venkitaraman, A.R. (2008). HP1-beta mobilization promotes chromatin changes that initiate the DNA damage response. Nature *453*, 682–686. https://doi.org/10.1038/nature06875.

Bakircioglu, M., Carvalho, O.P., Khurshid, M., Cox, J.J., Tuysuz, B., Barak, T., Yilmaz, S.,

Caglayan, O., Dincer, A., Nicholas, A.K., et al. (2011). The essential role of centrosomal NDE1 in human cerebral cortex neurogenesis. Am. J. Hum. Genet. *88*, 523–535. https://doi.org/10.1016/j.ajhg.2011.03.019.

Benetti, R., Gonzalo, S., Jaco, I., Schotta, G., Klatt, P., Jenuwein, T., and Blasco, M.A. (2007). Suv4-20h deficiency results in telomere elongation and derepression of telomere recombination. J. Cell Biol. *178*, 925–936. https://doi.org/10.1083/jcb.200703081.

Bierhoff, H., Dammert, M.A., Brocks, D., Dambacher, S., Schotta, G., and Grummt, I. (2014). Quiescence-induced LncRNAs trigger H4K20 trimethylation and transcriptional silencing. Mol. Cell *54*, 675–682. https://doi.org/10.1016/j.molcel.2014.03.032.

Bromberg, K.D., Mitchell, T.R.H., Upadhyay, A.K., Jakob, C.G., Jhala, M.A., Comess, K.M., Lasko, L.M., Li, C., Tuzon, C.T., Dai, Y., et al. (2017). The SUV4-20 inhibitor A-196 verifies a role for epigenetics in genomic integrity. Nat. Chem. Biol. *13*, 317–324. https://doi.org/10.1038/nchembio.2282.

Craig, J.M. (2005). Heterochromatin–many flavours, common themes. Bioessays *27*, 17–28. https://doi.org/10.1002/bies.20145.

Feng, Y., Olson, E.C., Stukenberg, P.T., Flanagan, L.A., Kirschner, M.W., and Walsh, C.A. (2000). LIS1 regulates CNS lamination by interacting with mNudE, a central component of the centrosome. Neuron *28*, 665–679. https://doi.org/10.1016/s0896-6273(00)00145-8.

Feng, Y., and Walsh, C.A. (2004). Mitotic spindle regulation by Nde1 controls cerebral cortical size. Neuron *44*, 279–293. https://doi.org/10.1016/j.neuron.2004.09.023.

Fraga, M.F., Ballestar, E., Villar-Garea, A., Boix-Chornet, M., Espada, J., Schotta, G., Bonaldi, T., Haydon, C., Ropero, S., Petrie, K., et al. (2005). Loss of acetylation at Lys16 and trimethylation at Lys20 of histone H4 is a common hallmark of human cancer. Nat. Genet. *37*, 391–400. https://doi.org/10.1038/ng1531.

Gatti, M., Pinato, S., Maspero, E., Soffientini, P., Polo, S., and Penengo, L. (2012). A novel ubiquitin mark at the N-terminal tail of histone H2As targeted by RNF168 ubiquitin ligase. Cell Cycle *11*, 2538–2544. https://doi.org/10.4161/cc.20919.

Gershman, A., Sauria, M.E.G., Guitart, X., Vollger, M.R., Hook, P.W., Hoyt, S.J., Jain, M., Shumate, A., Razaghi, R., Koren, S., et al. (2022). Epigenetic patterns in a complete human genome. Science *376*, eabj5089. https://doi.org/10.1126/science.abj5089.

Guenatri, M., Bailly, D., Maison, C., and Almouzni, G. (2004). Mouse centric and pericentric satellite repeats form distinct functional heterochromatin. J. Cell Biol. *166*, 493–505. https://doi.org/10.1083/jcb.200403109.

Guo, Y., Chomiak, A.A., Hong, Y., Lowe, C.C., Chan, W.-C., Andrade, J., Pan, H., Zhou, X., Berezovski, E., Monuki, E.S., et al. (2021). Histone H2A ubiquitination resulting from Brap loss of function connects multiple aging hallmarks and accelerates neurodegeneration. Preprint at bioRxiv. https://doi.org/10.1101/2020.10.22.341784.

Guven, A., Gunduz, A., Bozoglu, T.M., Yalcinkaya, C., and Tolun, A. (2012). Novel NDE1 homozygous mutation resulting in microhydranencephaly and not microlyssencephaly. Neurogenetics *13*, 189–194. https://doi.org/10.1007/s10048-012-0326-9.

Hahn, M., Dambacher, S., Dulev, S., Kuznetsova, A.Y., Eck, S., Worz, S., Sadic, D., Schulte, M., Mallm, J.P., Maiser, A., et al. (2013). Suv4-20h2 mediates chromatin compaction and is important for cohesin recruitment to heterochromatin. Genes Dev. *27*, 859–872. https://doi.org/10.1101/gad.210377.112.

Hannes, F.D., Sharp, A.J., Mefford, H.C., de Ravel, T., Ruivenkamp, C.A., Breuning, M.H., Fryns, J.P., Devriendt, K., Van Buggenhout, G., Vogels, A., et al. (2009). Recurrent reciprocal deletions and duplications of 16p13.11: the deletion is a risk factor for MR/MCA while the duplication may be a rare benign variant. J. Med. Genet. *46*, 223–232. https://doi.org/10.1136/jmg.2007.055202.

Houlihan, S.L., and Feng, Y. (2014). The scaffold protein Nde1 safeguards the brain genome during S phase of early neural progenitor differentiation. Elife *3*, e03297. https://doi.org/10.7554/elife.03297.

Hoyt, S.J., Storer, J.M., Hartley, G.A., Grady, P.G.S., Gershman, A., de Lima, L.G., Limouse, C., Halabian, R., Wojenski, L., Rodriguez, M., et al. (2022). From telomere to telomere: the transcriptional and epigenetic state of human repeat elements. Science *376*, eabk3112. https://doi.org/10.1126/science.abk3112.

Ingason, A., Rujescu, D., Cichon, S., Sigurdsson, E., Sigmundsson, T., Pietiläinen, O.P.H., Buizer-Voskamp, J.E., Strengman, E., Francks, C., Muglia, P., et al. (2011). Copy number variations of chromosome 16p13.1 region associated with schizophrenia. Mol. Psychiatry *16*, 17–25. https://doi.org/10.1038/mp.2009.101.

Jorgensen, S., Schotta, G., and Sorensen, C.S. (2013). Histone H4 lysine 20 methylation: key player in epigenetic regulation of genomic integrity. Nucleic Acids Res. *41*, 2797–2806. https://doi.org/10.1093/nar/gkt012.

Kidder, B.L., Hu, G., Cui, K., and Zhao, K. (2017). SMYD5 regulates H4K20me3-marked heterochromatin to safeguard ES cell self-renewal and prevent spurious differentiation. Epigenetics Chromatin *10*, 8. https://doi.org/10.1186/s13072-017-0115-7.

Kimura, H., Tsuboi, D., Wang, C., Kushima, I., Koide, T., Ikeda, M., Iwayama, Y., Toyota, T., Yamamoto, N., Kunimoto, S., et al. (2015). Identification of rare, single-nucleotide mutations in NDE1 and their contributions to schizophrenia susceptibility. Schizophr. Bull. *41*, 744–753. https://doi.org/10.1093/schbul/sbu147.

Lanctot, A.A., Guo, Y., Le, Y., Edens, B.M., Nowakowski, R.S., and Feng, Y. (2017). Loss of Brap results in premature G1/S phase transition and impeded neural progenitor differentiation. Cell Rep. *20*, 1148–1160. https://doi.org/10.1016/j.celrep.2017.07.018.

Lanctot, A.A., Peng, C.Y., Pawlisz, A.S., Joksimovic, M., and Feng, Y. (2013). Spatially dependent dynamic MAPK modulation by the Nde1-Lis1-Brap complex patterns mammalian CNS. Dev. Cell *25*, 241–255. https://doi.org/10.1016/j.devcel.2013.04.006.

Lander, E.S., Linton, L.M., Birren, B., Nusbaum, C., Zody, M.C., Baldwin, J., Devon, K., Dewar, K., Doyle, M., FitzHugh, W., et al. (2001). Initial sequencing and analysis of the human genome. Nature *409*, 860–921. https://doi.org/10.1038/35057062.

Larson, A.G., Elnatan, D., Keenen, M.M., Trnka, M.J., Johnston, J.B., Burlingame, A.L., Agard, D.A., Redding, S., and Narlikar, G.J. (2017). Liquid droplet formation by HP1α suggests a role for phase separation in heterochromatin. Nature *547*, 236–240. https://doi.org/10.1038/nature22822.

Li, S., Ku, C.Y., Farmer, A.A., Cong, Y.S., Chen, C.F., and Lee, W.H. (1998). Identification of a novel cytoplasmic protein that specifically binds to nuclear localization signal motifs. J. Biol. Chem. *273*, 6183–6189. https://doi.org/10.1074/jbc.273.11.6183.

Linhoff, M.W., Garg, S.K., and Mandel, G. (2015). A high-resolution imaging approach to investigate chromatin architecture in complex tissues. Cell *163*, 246–255. https://doi.org/10.1016/j.cell.2015.09.002.

Liu, Y., Rusinol, A., Sinensky, M., Wang, Y., and Zou, Y. (2006). DNA damage responses in progeroid syndromes arise from defective maturation of prelamin A. J. Cell Sci. *119*, 4644–4649. https://doi.org/10.1242/jcs.03263.

Marion, R.M., Strati, K., Li, H., Tejera, A., Schoeftner, S., Ortega, S., Serrano, M., and Blasco, M.A. (2009). Telomeres acquire embryonic stem cell characteristics in induced pluripotent stem cells. Cell Stem Cell *4*, 141–154. https://doi.org/10.1016/j.stem.2008.12.010.

Matheny, S.A., Chen, C., Kortum, R.L., Razidlo, G.L., Lewis, R.E., and White, M.A. (2004). Ras regulates assembly of mitogenic signalling complexes through the effector protein IMP. Nature *427*, 256–260. https://doi.org/10.1038/nature02237.

Nagamani, S.C.S., Erez, A., Bader, P., Lalani, S.R., Scott, D.A., Scaglia, F., Plon, S.E., Tsai, C.H., Reimschisel, T., Roeder, E., et al. (2011). Phenotypic manifestations of copy number variation in chromosome 16p13.11. Eur. J. Hum. Genet. *19*, 280–286. https://doi.org/10.1038/ejhg.2010.184.

Nelson, D.M., Jaber-Hijazi, F., Cole, J.J., Robertson, N.A., Pawlikowski, J.S., Norris, K.T., Criscione, S.W., Pchelintsev, N.A., Piscitello, D., Stong, N., et al. (2016). Mapping H4K20me3 onto the chromatin landscape of senescent cells indicates a function in control of cell senescence and tumor suppression through preservation of genetic and epigenetic stability. Genome Biol. *17*, 158. https://doi.org/10.1186/s13059-016-1017-x.

Noma, K.I., Allis, C.D., and Grewal, S.I.S. (2001). Transitions in distinct histone H3 methylation patterns at the heterochromatin domain boundaries. Science *293*, 1150–1155. https://doi.org/10.1126/science.1064150.

Nurk, S., Koren, S., Rhie, A., Rautiainen, M., Bzikadze, A.V., Mikheenko, A., Vollger, M.R.,

Altemose, N., Uralsky, L., Gershman, A., et al. (2022). The complete sequence of a human genome. Science *376*, 44–53. https://doi.org/10.1126/science.abj6987.

Paciorkowski, A.R., Keppler-Noreuil, K., Robinson, L., Sullivan, C., Sajan, S., Christian, S.L., Bukshpun, P., Gabriel, S.B., Gleeson, J.G., Sherr, E.H., and Dobyns, W.B. (2013). Deletion 16p13.11 uncovers NDE1 mutations on the non-deleted homolog and extends the spectrum of severe microcephaly to include fetal brain disruption. Am. J. Med. Genet. A *161*, 1523–1530. https://doi.org/10.1002/ajmg.a.35969.

Pawlisz, A.S., and Feng, Y. (2011). Three-dimensional regulation of radial glial functions by Lis1-Nde1 and dystrophin glycoprotein complexes. PLoS Biol. *9*, e1001172. https://doi.org/10.1371/journal.pbio.1001172.

Ramalingam, A., Zhou, X.G., Fiedler, S.D., Brawner, S.J., Joyce, J.M., Liu, H.Y., and Yu, S. (2011). 16p13.11 duplication is a risk factor for a wide spectrum of neuropsychiatric disorders. J. Hum. Genet. *56*, 541–544. https://doi.org/10.1038/jhg.2011.42.

Rauch, A., Thiel, C.T., Schindler, D., Wick, U., Crow, Y.J., Ekici, A.B., van Essen, A.J., Goecke, T.O., Al-Gazali, L., Chrzanowska, K.H., et al. (2008). Mutations in the pericentrin (PCNT) gene cause primordial dwarfism. Science *319*, 816–819. https://doi.org/10.1126/science.1151174.

Richards, E.J., and Elgin, S.C. (2002). Epigenetic codes for heterochromatin formation and silencing. Cell *108*, 489–500. https://doi.org/10.1016/s0092-8674(02)00644-x.

Roberts, S.A., and Gordenin, D.A. (2014). Hypermutation in human cancer genomes: footprints and mechanisms. Nat. Rev. Cancer *14*, 786–800. https://doi.org/10.1038/nrc3816.

Rossi, L.N., Candini, G., Scarlatti, G., Rossi, G., Prina, E., and Alberti, S. (1987). Autosomal dominant microcephaly without mental retardation. Am. J. Dis. Child. *141*, 655–659. https://doi.org/10.1001/archpedi.1987.04460060071037.

Ryu, T., Spatola, B., Delabaere, L., Bowlin, K., Hopp, H., Kunitake, R., Karpen, G.H., and Chiolo, I. (2015). Heterochromatic breaks move to the nuclear periphery to continue recombinational repair. Nat. Cell Biol. *17*, 1401–1411. https://doi.org/10.1038/ncb3258.

Saksouk, N., Simboeck, E., and Dejardin, J. (2015). Constitutive heterochromatin formation and transcription in mammals. Epigenetics Chromatin *8*, 3. https://doi.org/10.1186/1756-8935-8-3.

Scaffidi, P., and Misteli, T. (2005). Reversal of the cellular phenotype in the premature aging disease Hutchinson-Gilford progeria syndrome. Nat. Med. *11*, 440–445. https://doi.org/10.1038/nm1204.

Schindelin, J., Arganda-Carreras, I., Frise, E., Kaynig, V., Longair, M., Pietzsch, T., Preibisch, S., Rueden, C., Saalfeld, S., Schmid, B., et al. (2012). Fiji: an open-source platform for biological-image analysis. Nat. Methods *9*, 676–682. https://doi.org/10.1038/nmeth.2019.

Schotta, G., Lachner, M., Sarma, K., Ebert, A., Sengupta, R., Reuter, G., Reinberg, D., and Jenuwein, T. (2004). A silencing pathway to induce H3-K9 and H4-K20 trimethylation at constitutive heterochromatin. Genes Dev. *18*, 1251–1262. https://doi.org/10.1101/gad.300704.

Schotta, G., Sengupta, R., Kubicek, S., Malin, S., Kauer, M., Callen, E., Celeste, A., Pagani, M., Opravil, S., De La Rosa-Velazquez, I.A., et al. (2008). A chromatin-wide transition to H4K20 monomethylation impairs genome integrity and programmed DNA rearrangements in the mouse. Genes Dev. *22*, 2048–2061. https://doi.org/10.1101/gad.476008.

Schuster-Bockler, B., and Lehner, B. (2012). Chromatin organization is a major influence on regional mutation rates in human cancer cells. Nature *488*, 504–507. https://doi.org/10.1038/nature11273.

Shumaker, D.K., Lopez-Soler, R.I., Adam, S.A., Herrmann, H., Moir, R.D., Spann, T.P., and Goldman, R.D. (2005). Functions and dysfunctions of the nuclear lamin Ig-fold domain in nuclear assembly, growth, and Emery-Dreifuss muscular dystrophy. Proc. Natl. Acad. Sci. U S A *102*, 15494–15499. https://doi.org/10.1073/pnas.0507612102.

Solovei, I., Kreysing, M., Lanctot, C., Kosem, S., Peichl, L., Cremer, T., Guck, J., and Joffe, B. (2009). Nuclear architecture of rod photoreceptor cells adapts to vision in mammalian evolution. Cell *137*, 356–368. https://doi.org/10.1016/j.cell.2009.01.052.

Solovei, I., Thanisch, K., and Feodorova, Y. (2016). How to rule the nucleus: divide et impera. Curr. Opin. Cell Biol. *40*, 47–59. https://doi.org/10.1016/j.ceb.2016.02.014.

Solovei, I., Wang, A.S., Thanisch, K., Schmidt, C.S., Krebs, S., Zwerger, M., Cohen, T.V., Devys, D., Foisner, R., Peichl, L., et al. (2013). LBR and lamin A/C sequentially tether peripheral heterochromatin and inversely regulate differentiation. Cell *152*, 584–598. https://doi.org/10.1016/j.cell.2013.01.009.

Sridharan, R., Gonzales-Cope, M., Chronis, C., Bonora, G., McKee, R., Huang, C., Patel, S., Lopez, D., Mishra, N., Pellegrini, M., et al. (2013). Proteomic and genomic approaches reveal critical functions of H3K9 methylation and heterochromatin protein-1γ in reprogramming to pluripotency. Nat. Cell Biol. *15*, 872–882. https://doi.org/10.1038/ncb2768.

Strom, A.R., Emelyanov, A.V., Mir, M., Fyodorov, D.V., Darzacq, X., and Karpen, G.H. (2017). Phase separation drives heterochromatin domain formation. Nature *547*, 241–245. https://doi.org/10.1038/nature22989.

Takahashi, T., Nowakowski, R.S., and Caviness, V.S., Jr. (1993). Cell cycle parameters and patterns of nuclear movement in the neocortical proliferative zone of the fetal mouse. J. Neurosci. *13*, 820–833. https://doi.org/10.1523/jneurosci.13-02-00820.1993.

Takei, Y., Zheng, S., Yun, J., Shah, S., Pierson, N., White, J., Schindler, S., Tischbirek, C.H., Yuan, G.C., and Cai, L. (2021). Single-cell nuclear architecture across cell types in the mouse brain. Science *374*, 586–594. https://doi.org/10.1126/science.abj1966.

Talbert, P.B., and Henikoff, S. (2006). Spreading of silent chromatin: inaction at a distance. Nat. Rev. Genet. *7*, 793–803. https://doi.org/10.1038/nrg1920.

Thakur, J., Packiaraj, J., and Henikoff, S. (2021). Sequence, chromatin and evolution of satellite DNA. Int. J. Mol. Sci. *22*, 4309. https://doi.org/10.3390/ijms22094309.

Ting, D.T., Lipson, D., Paul, S., Brannigan, B.W., Akhavanfard, S., Coffman, E.J., Contino, G., Deshpande, V., Iafrate, A.J., Letovsky, S., et al. (2011). Aberrant overexpression of satellite repeats in pancreatic and other epithelial cancers. Science *331*, 593–596. https://doi.org/10.1126/science.1200801.

Tropeano, M., Ahn, J.W., Dobson, R.J., Breen, G., Rucker, J., Dixit, A., Pal, D.K., McGuffin, P., Farmer, A., White, P.S., et al. (2013). Male-biased autosomal effect of 16p13.11 copy number variation in neurodevelopmental disorders. PLoS One. *8*, e61365. https://doi.org/10.1371/journal.pone.0061365.

Uckelmann, M., and Sixma, T.K. (2017). Histone ubiquitination in the DNA damage response. DNA Repair (Amst) *56*, 92–101. https://doi.org/10.1016/j.dnarep.2017.06.011.

Ullmann, R., Turner, G., Kirchhoff, M., Chen, W., Tonge, B., Rosenberg, C., Field, M., Vianna-Morgante, A.M., Christie, L., Krepischi-Santos, A.C., et al. (2007). Array CGH identifies reciprocal 16p13.1 duplications and deletions that predispose to autism and/or mental retardation. Hum. Mutat. *28*, 674–682. https://doi.org/10.1002/humu.20546.

Vicient, C.M., and Casacuberta, J.M. (2017). Impact of transposable elements on polyploid plant genomes. Ann. Bot. *120*, 195–207. https://doi.org/10.1093/aob/mcx078.

Vissel, B., and Choo, K.H. (1989). Mouse major (γ) satellite DNA is highly conserved and organized into extremely long tandem arrays: implications for recombination between nonhomologous chromosomes. Genomics *5*, 407–414. https://doi.org/10.1016/0888-7543(89)90003-7.

Willems, M., Genevieve, D., Borck, G., Baumann, C., Baujat, G., Bieth, E., Edery, P., Farra, C., Gerard, M., Heron, D., et al. (2010). Molecular analysis of pericentrin gene (PCNT) in a series of 24 Seckel/microcephalic osteodysplastic primordial dwarfism type II (MOPD II) families. J. Med. Genet. *47*, 797–802. https://doi.org/10.1136/jmg.2009.067298.

Williams, N.M., Zaharieva, I., Martin, A., Langley, K., Mantripragada, K., Fossdal, R., Stefansson, H., Stefansson, K., Magnusson, P., Gudmundsson, O.O., et al. (2010). Rare chromosomal deletions and duplications in attention-deficit hyperactivity disorder: a genome-wide analysis. Lancet *376*, 1401–1408. https://doi.org/10.1016/s0140-6736(10)61109-9.

Wongtawan, T., Taylor, J.E., Lawson, K.A., Wilmut, I., and Pennings, S. (2011). Histone H4K20me3 and HP1α are late heterochromatin markers in development, but present in undifferentiated embryonic stem cells. J. Cell Sci. *124*, 1878–1890. https://doi.org/10.1242/jcs.080721.

Yang, L., Ma, Z., Wang, H., Niu, K., Cao, Y., Sun, L., Geng, Y., Yang, B., Gao, F., Chen, Z., et al. (2019). Ubiquitylome study identifies increased histone 2A ubiquitylation as an evolutionarily conserved aging biomarker. Nat. Commun. *10*, 2191. https://doi.org/10.1038/s41467-019-10136-w.

Yokoyama, Y., Matsumoto, A., Hieda, M., Shinchi, Y., Ogihara, E., Hamada, M., Nishioka, Y., Kimura, H., Yoshidome, K., Tsujimoto, M., and Matsuura, N. (2014). Loss of histone H4K20 trimethylation predicts poor prognosis in breast cancer and is associated with invasive activity. Breast Cancer Res. *16*, R66. https://doi.org/10.1186/bcr3681.

Zhu, Q., Hoong, N., Aslanian, A., Hara, T., Benner, C., Heinz, S., Miga, K.H., Ke, E., Verma, S., Soroczynski, J., et al. (2018). Heterochromatin-encoded satellite RNAs induce breast cancer. Mol. Cell *70*, 842–853.e7. https://doi.org/10.1016/j.molcel.2018.04.023.

STAR★METHODS

KEY RESOURCES TABLE

REAGENT or RESOURCE	SOURCE	IDENTIFIER
Antibodies		
Histone H4K20me3	Diagenode	Cat# C15410207; RRID: AB_2713909
Histone H4K20me3	Abcam	Cat# ab9053; RRID: AB_306969
Histone H4K20me3 clone 6F8-D9	Abcam	Cat# ab78517; RRID: AB_1951279
Histone H4K20me1 clone 5E10-D8	Abcam	Cat# ab78513; RRID: AB_2233105
Histone H4K5Ac	Abcam	Cat# ab51997; RRID: AB_2264109
Histone H4K8Ac	Abcam	Cat# ab45166; RRID: AB_732937
Histone H4K16Ac	Abcam	Cat# ab109463; RRID: AB_10858987
Histone H4	Active Motif	Cat# 39269; RRID: AB_2636967
Histone H4	GeneTex	Cat# GTX129560; RRID: AB_2886030
Histone H3K9me3	Abcam	Cat# ab8898; RRID: AB_306848
Histone H3K27me3	Diagenode	Cat# C15200181; RRID: AB_2819192
Histone H3K27me3	Active Motif	Cat# 39055; RRID: AB_2561020
Histone H3K36me3	Active Motif	Cat# 61902; RRID: AB_2615073
Histone H3K4me3	Diagenode	Cat# C15410003
Histone H3K9Ac, clone C5B11	Cell Signaling Technology	Cat# 9649; RRID: AB_823528
Histone H3.3	Novus Biologicals	Cat# NBP2-24697
Histone H3S10p	Millipore	Cat# 06-570; RRID: AB_310177
Histone H3	Active Motif	Cat# 61799; RRID: AB_2793771
Histone H3 (1G1)	Epigentek	Cat# A68386
Histone H2A	Cell Signaling Technology	Cat# 12349; RRID: AB_2687875
Histone H2A	Cell Signaling Technology	Cat# 2578; RRID: AB_2118804
Histone H2A, Clone C10037	MBL	Cat# D210-3; RRID: AB_591881
Histone H2A	GeneTex	Cat# GTX129418
Ubiquityl-Histone H2AK119	Cell Signaling Technology	Cat# 8240; RRID: AB_10891618
Ubiquityl-Histone H2A Clone E6C5	Millipore	Cat# 05-678; RRID: AB_11214408
phospho-Histone H2A.X (Ser139), clone JBW301	Millipore	Cat# 05-636; RRID: AB_309864
phospho-Histone H2A.X (Ser139)	Cell Signaling Technology	Cat# 2577; RRID: AB_2118010
phospho-Histone H2A.X (Ser139)	Bethyl Laboratories	Cat# IHC-00059-3
phospho-Histone H2A.X (Ser139) Clone 2F3	Biolegend	Cat# 613401; RRID: AB_315794
Histone H2A.Y/macroH2A.1	Cell Signaling Technology	Cat# 8551; RRID: AB_2797647
Histone H2A.Y/macroH2A.1 Clone 866416	Novus Biologicals	Cat# MAB8318
Histone H2B	Active Motif	Cat# 39125; RRID: AB_2793163
Ubiquityl-Histone H2B K120	Active Motif	Cat# 39623; RRID: AB_2793279
Lamin B1	Abcam	Cat# ab16048; RRID:AB_443298
Lamin B1 (M20)	Santa Cruz	Cat# sc-6217; RRID: AB_648158
Lamin A/C	Cell Signaling Technology	Cat# 4777; RRID: AB_10545756
Lamin A/C	BD Biosciences	Cat# 612162; RRID: AB_399533
UBF	Santa Cruz	Cat# sc-13125; RRID: AB_671403
Npm1	Abcam	Cat# ab10530; RRID: AB_297271
HP1α	Cell Signaling Technology	Cat# 2616; RRID: AB_2070987

(*Continued on next page*)

Continued

REAGENT or RESOURCE	SOURCE	IDENTIFIER
HP1β	Millipore	Cat# MAB3448; RRID: AB_2071096
HP1γ	Cell Signaling Technology	Cat# 2619; RRID: AB_2070984
Tuj1	Covance	Cat# MMS-435P; RRID: AB_2313773
Dcx	Proteintech	Cat# 13925-1-AP; RRID: AB_2088476
Pax6	Covance	Cat# PRB-278P; RRID: AB_291612
Sox2	Millipore	Cat# Ab5603; RRID: AB_2286686
IdU	BD Biosciences	Cat# 347580; RRID: AB_10015219
CldU	Abcam	Cat# Ab6326 ; RRID: AB_305426
NDE1/Nde1 rabbit polyclonal against full-length NDE1	Proteintech	Cat# 10233-1-AP; RRID: AB_2149877
NDE1/Nde1 mouse monoclonal	Santa Cruz	Cat# sc100328; RRID: AB_2149881
NDE1/Nde1, rabbit polyclonal against N-terminus	Feng et al., 2000	https://www.sciencedirect.com/science/article/pii/S0896627300001458?via%3Dihub
Smc3	Bethyl Laboratories	Cat# A300-480A
Smc3	Abcam	Cat# ab9263; RRID: AB_307122
53 BP1	Novus Biologicals	Cat# NB100-304
Brca1	Santa Cruz	Cat# sc-642; RRID: AB_630944
Brca1	Novus Biologicals	Cat# MAB22101
Brca1 (clone 8F7)	Novus Biologicals	Cat# NBP1-41186
Iba	Wako	Cat# 019-19741; RRID: AB_839504
CD68 (KP1)	Abcam	Cat# ab955; RRID: AB_307338
CD68 (FA-11)	Abcam	Cat# ab53444; RRID: AB_869007
GFAP	Abcam	Cat# ab7260; RRID: AB_305808
GFAP (GA5)	Novus Biologicals	Cat# NBP2-29415
Phospho-Tau (Thr181) 5H9L11	Thermo Fisher	Cat# 701530; RRID: AB_2532491
Phospho-Tau (Ser416) D7U2P	Cell Signaling Technology	Cat# 15013; RRID: AB_2728782
Phospho-Tau (Thr 217)	GenScript	Cat# A00896; RRID: AB_2622113
Phospho-Tau (Ser396)	GenScript	Cat# A01387; RRID: AB_1575880
Tau (Tau 46)	Santa Cruz	Cat# sc32274; RRID: AB_628327
Tau (A10)	Santa Cruz	Cat# sc-390476
Tau (TAU-5)	Santa Cruz	Cat# sc-58860; RRID: AB_785931
NeuN	Cell Signaling Technology	Cat# 24307; RRID: AB_2651140
NeuN, Clone A60	Millipore	Cat# MAB377; RRID:AB_2298772
Ubiquitin, Clone Ubi-1	Millipore	Cat# MAB1510; RRID: AB_2180556
Ubiquitin (Ubi-1)	Novus Biologicals	Cat# NB300-130
GAPDH	Sigma	Cat# G9295; RRID: AB_1078992
Actin	Sigma	Cat# A2668; RRID: AB_258014
Tubulin, alpha, clone B-5-1-2	Sigma	Cat# T6074; RRID: AB_477582
Vinculin	Sigma	Cat# V9131; RRID: AB_477629
Myosin	Cell Signaling Technology	Cat# 3403; RRID: AB_2147297
Biological samples		
Human postmortem cerebral cortex paraffin sections	NIH NeuroBioBank	HCTTA
Human postmortem cerebral cortex paraffin sections	NIH NeuroBioBank	HCTRY

(*Continued on next page*)

Continued

REAGENT or RESOURCE	SOURCE	IDENTIFIER
Human postmortem cerebral cortex paraffin sections	NIH NeuroBioBank	HCTPC
Chemicals, peptides, and recombinant proteins		
Formaldehyde, EM grade	Ted Pella	Cat# 18505
Glutaraldehyde, EM grade	Ted Pella	Cat# 18421
Disuccinimidyl glutarate	Thermo Fisher	Cat# A35392
5-Iodo-2′-deoxyuridine	Sigma	Cat# I7125
5-Chloro-2′-deoxyuridine	Sigma	Cat# C6891
A-196	MedChemExpress	Cat# HY-100201
N-Ethylmaleimide	Pierce	Cat# 23030
Iodoacetamide	Sigma	Cat# I1149
Leupeptin	Thermo Fisher	Cat# 78435
Pepstatin A	Thermo Fisher	Cat# 78436
Aprotinin	Sigma	Cat# A6103
Benzamidine	Sigma	Cat# 434760
Phenylmethanesulfonyl fluoride	Sigma	Cat# P7626
MG-132	selleckchem	Cat# S2619
TRIzol Reagent	Invitrogen	Cat# 15596018
cOmplete™, Mini, EDTA-free Protease Inhibitor Cocktail	Roche	Cat# 11836170001
NorthernMax Hybridization Buffer	Ambion	Cat# AM8677
PCR DIG Probe Synthesis Kit	Roche	Cat# 11636090910
CSPD ready-to-use	Roche	Cat# 11755633001
PCR Fluorescein Labeling Mix	Roche	Cat# 11636154910
Sodium Cacodylate Buffer	EM Science	Cat# 11653
Osmium Tetroxide	EM Science	Cat# 19110
Antigen unmasking solution	Vector Lab	Cat# H-3300
Critical commercial assays		
20S Proteasome Assay Kit	Millipore	Cat# APT280
FD Rapid GolgiStain kit	FD Neuro Technologies	Cat# PK401
Experimental models: Cell lines		
COS-7	ATCC	Cat# CRL-1651
XCL-1 NSC	XCell Science	Cat# SC-001-1V
Experimental models: Organisms/strains		
Nde1 KO mice	Feng and Walsh, 2004	https://www.sciencedirect.com/science/article/pii/S0896627304006117?via%3Dihub
Brap KO mice	Lanctot et al., 2013	https://www.sciencedirect.com/science/article/pii/S1534580713002177
Brap floxed mice	Lanctot et al., 2017	https://www.sciencedirect.com/science/article/pii/S2211124717309713?via%3Dihub
p53 KO mice, B6.129S2-*Trp53*^{tm1Tyj}/J	JaxMice	Cat# 002101
p53 floxed mice, B6.129P2-*Trp53*^{tm1Brn}/J	JaxMice	Cat# 008462
Emx1-Cre mice, B6.129S2-*Emx1*$^{tm1(cre)Krj}$/J	JaxMice	Cat# 005628

(*Continued on next page*)

Continued

REAGENT or RESOURCE	SOURCE	IDENTIFIER
Oligonucleotides		
PCR primers	IDT	See Table S2 for a list of oligonucleotides
Recombinant DNA		
EGFP-Nde1 plasmid in pEGFP-1 vector	Feng et al., 2000	https://www.sciencedirect.com/science/article/pii/S0896627300001458?via%3Dihub
Brap plasmid in pCMV-SPORT 6 vector	ATCC	dbEST ID 16438671
pγSat plasmid	Lundgren et al. Cell. 2000 Nov 22;103(5):733-43	Addgene Plasmid #39238
Software and algorithms		
Image-ProPremier	Media Cybernetics	https://www.mediacy.com/support/imagepropremier
ImageJ	ImageJ	https://imagej.nih.gov/ij/
GraphPad Prism	GraphPad	https://www.graphpad.com/scientific-software/prism/

RESOURCE AVAILABILITY

Lead contact

Further information and requests for resources and reagents should be directed to, and will be fulfilled by the lead contact, Yuanyi Feng (yuanyi.feng@usuhs.edu).

Materials availability

This study did not generate new unique reagents. The NDE1 N-terminal antibody is available upon request, but with restrictions due to difficulties in generating the peptide for affinity purification. Other unique/stable reagents used in this study are available from the Lead contact with a completed Materials Transfer Agreement.

Data and code availability

The current study does not generate new dataset to be deposited in the public repository. Any additional information required to reanalyze the data reported in this paper is available from the lead contact upon request.

EXPERIMENTAL MODEL AND SUBJECT DETAILS

Mice

Nde1 knockout ($Nde1^{-/-}$), Brap knockout ($Brap^{-/-}$), and Brap floxed ($Brap^{flox/flox}$) mice were generated by conventional mouse embryonic stem cell-based gene targeting (Feng and Walsh, 2004; Lanctot et al., 2013, 2017). The Trp53 knockout ($p53^{-/-}$) and floxed ($p53^{flox/flox}$) mice were purchased from JaxMice (stock # 002101 and # 008462, respectively). Emx1-Cre mice were purchased from JaxMice (stock # 005628). $Nde1^{-/-}P53^{-/-}$, $Nde1^{-/-}p53^{cKO}$, and $Nde1^{-/-}Brap^{cKO}$ mice were generated by crossing $Nde1^{+/-}$ mice with $P53^{-/-}$, $p53^{flox/flox}$, $Brap^{flox/flox}$, and Emx1-Cre mice. All mice used for this study were housed and bred according to the guidelines approved by the IACUC committees of Northwestern University and Uniformed Services University of Health Services in compliance with the AAALAC's guidelines. Both male and female mice were analyzed. Ages of study are from embryonic day 12.5 (E12.5) to one year. Experiments were performed using littermates or age and genetic background matched control and mutant groups in both sexes. For timed matings, the day of vaginal plug was considered E0.5.

Human cerebral cortical tissue samples

Paraffin sections of human postmortem cortical tissue were obtained from the NIH NeuroBioBank at the University of Miami through a material transfer agreement and were analyzed in compliance with

NeuroBioBank ethical guidelines. Three neurologically normal individuals (HCTTA, HCTRY, and HCTPC) who died between the ages of 29 and 33 of cardiovascular causes were analyzed.

Cell culture

The NCRM-1/XCL-1 human neural stem cells (NSCs), derived from the human induced pluripotent stem cell (hiPSC) line NCRM-1, were obtained through a material transfer agreement with the National Institutes of Health Center for Regenerative Medicine. These cells were generated through collaboration with the NIH, Sigma-Aldrich, and XCell Sciences from CD 34^+ human cord blood cells by episomal plasmid reprogramming. They were differentiated to NSCs through an embryoid body (EB) method by XCell Sciences, are commercially available as XCL-1 NSCs. COS-7 cells were from ATCC.

METHOD DETAILS

Cell culture, transfection, and fluorescence microscopy

Mouse neural stem/progenitor cells were isolated from embryonic cortices at E12.5. Single cells were prepared and cultured in DMEM/F12 with N2 and B27 supplements, Penicillin-Streptomycin, Glutamine, Heparin, and growth factors (20 ng/ml EGF and 10 ng/mL FGF) at 37°C in 5% CO2. Cultures were inspected daily and split 1:3 to 1:5 every 3 days depending on cell density and speed of growth. The A-196 inhibitor (MedChemExpress) was dissolved in DMSO and added to the culture medium at a final concentration of 4 uM or 10 uM for 3 days. Then cells were collected for total protein extraction and IB analyses. Control cells were treated with DMSO alone.

Human NSCs were cultured on Matrigel-coated glass coverslips in DMEM/F12 supplemented with 1.0% N2 and 2.0% B27 supplements and 40 μL/mL bFGF.

Cos7 cells from ATCC were cultured in DMEM supplemented with 10% fetal bovine serum. cDNA transfection was performed using Lipofectamine 2000 (Invitrogen) following manufacturer's instructions. cDNA plasmids of GFP-Nde1 was modified by replacing the tubulin coding region of EGFP-Tubulin plasmid (Clontech) with full length Nde1 cDNA, and the full-length Brap plasmid was purchased as an expressed sequence tag (EST) clone from the ATCC(Feng et al., 2000; Lanctot et al., 2017). Immunofluorescence cell staining was carried out by fixing with 4% EM grade formaldehyde, blocked in 1% BSA and 5mg/ml lysine, and immuno-stained in a buffer containing 25 mM Hepes, pH 7.4, 250 mM Sucrose, 25 mM KCl, 25mMMg$(CH_3COO)_2$, 1% BSA, and 0.25% Saponin.

Superresolution immunofluorescence images were recorded on a Zeiss 980 confocal equipped with an Airyscan2 area detector (Zeiss Microscopy, Jena, Germany) imaging in super-resolution mode (40nm/pixel sampling resolution). Image stacks were processed in Zeiss Zen software to produce final super-resolution images.

Time-lapse fluorescence microscopy

For time-lapse imaging of GFP-Nde1, transfected cells grown in phenol red-free DMEM and 10% FBS on coverslips were assembled into a Pecon POC-R2 chamber (PeCon GmbH, Erbach, Germany). This chamber was maintained at 37°C and 5% CO_2 for the duration of the experiment. The chamber was placed on a Leica DMI 6000B inverted microscope controlled by Leica LAS X software (Leica Microsystems, Inc., Buffalo Grove, IL). Images of selected cells were recorded at 40x magnification using both transmitted light (using differential interference contrast [DIC]) and fluorescent light (through a filter cube appropriate for GFP) either every 10 seconds for a duration of 15 minutes or every 10 minutes for a period of 16 hours.

Fluorescence recovery after photo-bleaching (FRAP)

For FRAP experiments, GFP-Nde1 transfected cells grown in phenol red-free DMEM and 10% FBS on coverslips were assembled into a Pecon POC-R2 chamber (PeCon GmbH, Erbach, Germany). This chamber was maintained at 37°C and 5% CO_2 for the duration of the experiment. The chamber was placed on a Zeiss 700 confocal microscope (Zeiss Microscopy, Jena, Germany) and images were recorded using Zeiss Zen software using settings appropriate for GFP. Selected cells were imaged at 10x magnification. A small region in either the cytoplasm or nucleus was then bleached using the bleaching function of the software and subsequent images were recorded at intervals ranging from 5 to 15 seconds. For intensity analysis of bleached regions, image sequences were imported into FIJI (Schindelin et al., 2012). Regions of interest

(ROIs) were defined in FIJI with care so that even if the area to be measured moved over the duration of the experiment, the measured area was always completely filled with fluorescence. Numerical measures of pixel intensity were then imported into Microsoft Excel for analysis (Microsoft, Inc., Redmond, WA)

Immunoblotting

Immunoblotting of total cell or tissue proteins was performed by extracting with boiling 2XSDS PAGE sample buffer (62.5 mM Tris-HCl, pH 6.8, 2.5% SDS, 0.7135 M β-mercaptoethanol, 10% glycerol, 0.002% Bromophenol Blue) to fully dissolve the tissue proteins, heating at 95°C for 10 min to ensure protein denaturation, and passing through syringes with a $29^{1/2}$ gauge needle three times to sheer nuclear DNA and obtain homogenous extracts. 10-30 ug of proteins were loaded on the gel for immunoblotting analysis. Loadings were adjusted and normalized by the total protein content according to Coomassie blue stain of the gel after SDS PAGE and by the level of housekeeping proteins. Quantification of bands was performed using ImageJ software and normalized to Ponceau S or housekeeping proteins.

Histone extractions

Cell or tissues were re-suspended or homogenized and lysed in PBS containing 0.5% Triton X100, 25 ug/ml leupeptin, 10 ug/ml Pepstatin A, 5 ug/ml Aprotinin, 10 mM Benzamidine, 2 mM PMSF, 10mM *N*-Ethylmaleimide (NEM), 10 mM iodoacetamide (IAA), and 0.02% NaN_3 at a density of ~10^7 cells/ml. Nuclei were first collected by centrifuge at 600 x g for 10min at 4°C, washed once, and re-suspended in 0.2 N HCl at a density of 4x10^7 nuclei per ml to extract histones overnight at 4°C. After clearing debris by centrifugation at 16,000 x g for 10 min at 4°C, the histone containing supernatants were neutralized with 2 M Tris Base. Protein concentration was determined by measuring absorbance at 280 nm. Extracted histones were stored in aliquots at -20°C.

Immunohistological analyses

Immunofluorescence staining of brain tissue sections was carried out by fixing mouse brains with transcardial perfusion with PBS and 4% paraformaldehyde and then processed in 12 um cryosections or 5 um paraffin sections. After treating with antigen unmasking solutions (Vector Labs), brain sections were blocked with 5% goat serum and incubated with primary antibodies in PBS, 0.1% Triton X-100, and 5% goat serum at 4°C overnight, and followed by staining with fluorescence conjugated secondary antibodies and Hoechst 33342. Epifluorescence images were acquired with a Leica CTR 5500 fluorescence, DIC, and phase contrast microscope equipped with the Q Imaging Regita 2000R digital camera. Images were imported to Adobe Photoshop and adjusted for brightness and black values.

Ultra-structural analysis

Mouse embryos were fixed in 2% glutaraldehyde and adult mouse brains were fixed with EM grade formaldehyde (2%) and glutaraldehyde (2%) in PBS by transcardial perfusion. The neocortex of perfused brains were dissected and cut to pieces of <1 mm^3 in size which were immersed in the same fixative overnight and then washed three times in PBS. Samples were then washed 3x 15min in cacoldylate buffer (CB, 0.1M, pH 7.4) to remove phosphate ions and subsequently immersed in 2% OsO_4 in CB for 1 hour. Following 3x15 min washes in CB, samples were dehydrated in a graduated series of ethanol, infiltrated with Spurr's epoxy resin (Electron Microscopy Sciences, Hatfield, PA), and polymerized at 70°C for 10 hours. Thin sections (70-90nm) were cut on a Leica Ultracut UC-6 ultramicrotome (Leica Microsystems, Wetzlar, Germany). Sections were collected on 3mm copper grids and subsequently stained for 30min with 2% aqueous uranyl acetate and for 5min with Reynold's lead citrate. Embryonic brain specimens were examined with a JEOL 1220 transmission electron microscope equipped with Kodak digital camera. Adult brain specimens were examined with a JEOL JEM-1011 transmission electron microscope equipped with an Advanced Microscopy Techniques 4MP digital camera (AMT Corp). Celltype identities in embryonic cortices were determined based on the location of the cells, in which NPCs were in the ventricular zone and neurons were in the cortical plate. Neurons in adult brains were identified by their pale cytoplasm and a larger, round, and euchromatin-rich nucleus.

Golgi-cox staining and dendritic spine analysis

Mice were euthanized with CO_2; brains were quickly dissected, rinsed with deionized water, immersed in impregnation solution, and processed using FD Rapid GolgiStain kit (FD NeuroTechnologies) according to manufacturer's instructions. Stained sections were examined under a Leica DM5000 light microscope.

Pyramidal neurons in the cerebral cortex and hippocampus regions were imaged with 40x objective and photographed. For dendritic spine density analysis, 16-20 pyramidal neurons in neocortical layer II/III of each mouse were randomly selected for assessment. The number of spines per 10 micrometers in secondary apical dendrites (branched from primary dendrites arising from the soma) was scored using the NIH ImageJ software.

Nucleotide administration and S-phase analysis

To perform S-phase analysis, pregnant mice were injected intraperitoneally with 50 mg/kg of thymidine analogue IdU followed by thymidine analogue CldU 90 min after IdU injection. Then mice were euthanized 30 min after CldU injection for embryo extraction and histological preparation. Early S-phase cells were identified by CldU+ IdU- labeling. Mid S-phase cells were identified by CldU and IdU double labeling. Cells in late S-phase and G2-phase were identified by IdU+ CldU- labeling.

Chromatin immunoprecipitation

Cerebral cortical tissue was dissected from wild type embryos at E12.5, fixed for 30 minutes in 2 mM disuccinimidyl glutarate and then for 10 minutes in 1% formaldehyde. Fixed tissue was suspended in 50mM Tris-HCl pH 8.0, 150 mM NaCl, 5 mM EDTA, and 0.5% NP40, supplemented with 1mM PMSF and 1X Roche protease inhibitor mix to isolate nuclei. Isolated nuclei were sonicated using a Diagenode Bioruptor to reduce the DNA fragment size to an average of 200-1000 bp. After the removal of insoluble cell debris, 10ul of sheared chromatin was removed to determine the amount of input, and the rest were divided to three equal parts and incubated with antibodies against Nde1, Smc3, and a non-specific negative control IgG, respectively. After overnight incubation at 4°C, the immuno-complexes were precipitated with M280 paramagnetic beads (ThermoFisher) coated with anti-rabbit IgG and pre-blocked with 0.5% BSA. The immunoprecipatates were washed sequentially with low-salt buffer (50mM Tris-HCl pH 8.0, 5mM EDTA, 150mM NaCl for three times, high-salt buffer (50mM Tris-HCl pH 8.0, 5mM EDTA, 500mM NaCl) once, and LiCl buffer (10mM Tris-HCl pH8.0, 1mM EDTA, 250mM LiCl, 0.5% NP40, and 0.5% Na-deoxycholate) once. The immunoprecipitated chromatin was eluted with 100mM NaHCO3 and 1% SDS. Protein-DNA cross-linking was reversed by incubating at 65°C in 200mM NaCl followed by RNase A and protease K digestions. The gDNA was purified by MinElute PCR purification columns (QIAGEN) and quantified by qPCR with StepOnePlus real-time PCR system (Applied Biosystems). The amount of gDNA in each immunoprecipitation is determined as % of total input.

Primer sequences for ChIP-qPCR are listed in Table S2, list of oligonucleotides.

Northern blot analysis

RNA was extracted from mouse cortical tissue using TRIzol reagent (Thermo Fisher) according to the manufacturer's protocol. After removing genomic DNA with TURBO DNase (Ambion), 2.5 ug of total RNA was mixed with formaldehyde and formamide denaturation buffer, incubated at 55°C for 15 min, and electrophoresed in a 1.2% agarose gel with 0.6M formaldehyde. RNA was transferred onto Amersham Hybond N+ membrane (GE) and crosslinked with ultraviolet light. The membrane was prehybridized in NorthernMax Hybridization Buffer (Ambion). Northern blot probe for major mouse satellite was generated by PCR of mouse genomic DNA with primers ATATTTCACGTCCTAAAGTGTG and GGCGAGGAAAACTGAAAAA G using the PCR DIG Probe Synthesis Kit (Roche). 0.1 nM probe was applied to the prehybridized membrane and hybridized in NorthernMax hybridization buffer (Ambion) at 42°C overnight. The membrane was washed twice with 2X SSC and 0.1% SDS for 15 min each at room temperature followed by washing with 0.2X SSC and 0.1% SDS at 65°C twice for 15 min each. Chemiluminescent detection of DIG signals on the membrane was performed using CSPD, ready-to-use (Roche) according to manufacturer's instructions.

Mouse major satellite genomic DNA analysis

Genomic DNA was isolated from mouse cortical tissue using genomic DNA extraction kit (QIAGEN). PCR amplifications of major satellite repeats were performed using primers ATATTTCACGTCCTAAAGTGTG and GGCGAGGAAAACTGAAAAAG.

The PCR products were cloned with the TOPO TA Cloning Dual Promoter Kit (Invitrogen). The resulting PCR clones were sequenced by Sanger sequencing using T7 and M13 reverse primers. 100 clones per

genotype were randomly selected for sequencing analysis. All clones containing major satellite sequences were included in the analysis.

ImmunoFISH analysis

Mouse brain sections (5um) on glass slides were de-paraffined and incubated in 10mM citric acid buffer at 95C for 30min. The slides were washed three times with PBS, treated with 0.1% Triton X100 in PBS for 15min and followed by two 2XSSC washes, a cold acetone treatment for 5 min, and three more 2X SSC washes for 5 min each at room temperature. Then the slides were treated or stored in 2XSSC and 50% formamide for longer than 4 hours.

The FISH probe for mouse major satellite DNA was amplified from the plasmid clone pγSat that contains eight copies of the 234bp mouse major satellite (γ-satellite) repeats using PCR Fluorescein Labeling Mix (Roche). Oligo primers used for PCR amplification are CGTGATTTTCAGTTTTCTCG and GGCGAGGAAAA CTGAAAAAG. Pretreated tissue slides were transferred to hybridization buffer containing 50% formamide, 20mM sodium phosphate pH7.0 and 2xSSC, co-denatured with 100ng of DNA probe per slide at 80°C for 5 minutes, followed by hybridization at 37°C for 48–72 hours. After hybridization, slides were washed three time with 2XSSC at 37°C for 5 min, three times with 0.1XSSC and 0.1% NP-40 at 60°C for 5 min, and once with 2XSSC at room temperature for 5 min. Then the slides were transferred to PBS and processed for immuno-histological stains.

20S proteasome assay

Proteasomes were extracted from mouse cortical tissue in a lysis buffer containing 50 mM HEPES, pH 7.5, 5 mM EDTA, 150 mM NaCl and 1% Triton X-100, 1 uM DTT and 2 mM ATP. Proteasome activities were determined using a 20S proteasome activity assay kit (Millipore APT280) according to manufacturer's instructions. The amount of cleaved AMC fragment of Suc-LLVY-AMC was quantified using a CLARIOstar Plus plate reader (BMG LABTECH) at excitation (EX) = 380/emission (EM) = 460. Reaction mixtures were incubated with 10 μM lactacystin or MG132 before addition of fluorogenic substrates to ensure the specificity of the assays.

QUANTIFICATION AND STATISTICAL ANALYSIS

No statistical methods were used to predetermine sample size, while all experiments were performed with a minimum of three biological replicates and all cell counts were obtained from at least ten random fields. The experiments were not randomized; the investigators were not blinded to the sample allocation and data acquisition during experiments but were blinded in quantitative image analyses using the Image-Pro-Premier (Media Cybernetics) and the NIH ImageJ software.

All statistical analyses were done using GraphPad Prism 9.0 software. Data were analyzed by unpaired two-tailed Student's t tests or by Kolmogorov-Smirnov tests for comparing differences between different genotypes. Statistical significance, denoted by asterisks with the corresponding p values or p values, is indicated in each figure legend. Differences were considered significant with a p value <0.05.